Development of a Beam Configuration for the SG4 Laser to Support both Direct and Indirect Drive

William Wang
Pittsford Sutherland High School
Pittsford, NY
Advisor: Dr. R. Stephen Craxton

Laboratory for Laser Energetics
University of Rochester
Rochester, NY

August 2020

Abstract

Recent papers (e.g., K. Lan et al. Phys. Plasmas 21, 010704 (2014)) have proposed "octahedral," or six-hole, hohlraums for the planned SG4 laser. Octahedral hohlraums aim to increase indirect drive uniformity on the capsule (compared with the cylindrical hohlraums currently used on the National Ignition Facility). The SG4 target chamber uses 48 quads (each quad is a group of 4 laser beams) to drive the octahedral hohlraum with 8 quads/hole. This work proposes an amended target chamber that will provide the option of direct drive along with indirect drive. A view-factor program, *LORE*, has been created for the purpose of calculating the capsule nonuniformity for indirect drive. *LORE* simulations have confirmed the results obtained by Lan et al. for octahedral hohlraums and predict a nonuniformity ranging from 0.44% at early times (when the capsule is irradiated primarily by x rays from the laser spots) to 0.11% at later times (when the heated hohlraum wall dominates). The beam pointings for direct drive have been optimized using the 2-D hydrodynamics simulation code *SAGE* such that an RMS nonuniformity of $\sim 1\%$ in the deposited laser energy can be achieved while beams are repointed by no more than 9°. Further improvements to the uniformity are expected with additional optimization. Experiments on the 60-beam OMEGA laser using a seven-hole hohlraum are proposed as a platform for studying uniformity in spherical hohlraums.

I Introduction

An important criterion for achieving ignition and gain through inertial confinement fusion (ICF) is obtaining high levels of uniformity on a spherical capsule [1]. The capsule contains two isotopes of hydrogen, deuterium and tritium, as fuel, which are held inside a shell typically made of plastic or glass. As the capsule shell heats to high temperatures, it turns to plasma, both ablating outwards and compressing inwards. This process compresses the fuel to high temperatures and densities, allowing the strong nuclear force to overcome the electrostatic force between the positively charged nuclei, and the deuterium and tritium fuse into a helium nucleus and release large amounts of energy, mostly in the form of energetic neutrons.

The two current approaches to laser-driven ICF are known as direct and indirect drive (Fig. 1). In direct drive, laser beams are pointed at the fuel capsule, and the capsule is directly irradiated by the beams. During indirect drive, the fuel capsule is placed inside of a case, known as a hohlraum, which is made of a high-Z material (typically gold). The laser beams enter the hohlraum through laser entrance holes (LEH's) and rather than directly irradiating the capsule, the beams deposit energy onto the hohlraum wall. The hohlraum wall then emits x rays, which irradiate the capsule and heat other parts of the hohlraum wall. Indirect drive is therefore less sensitive to small-scale nonuniformities on the laser beams, which are caused by imperfections in the laser beams. Indirect drive, however, is less energy efficient since only a small fraction of the laser power (often 10 to 20%) is absorbed by the capsule.

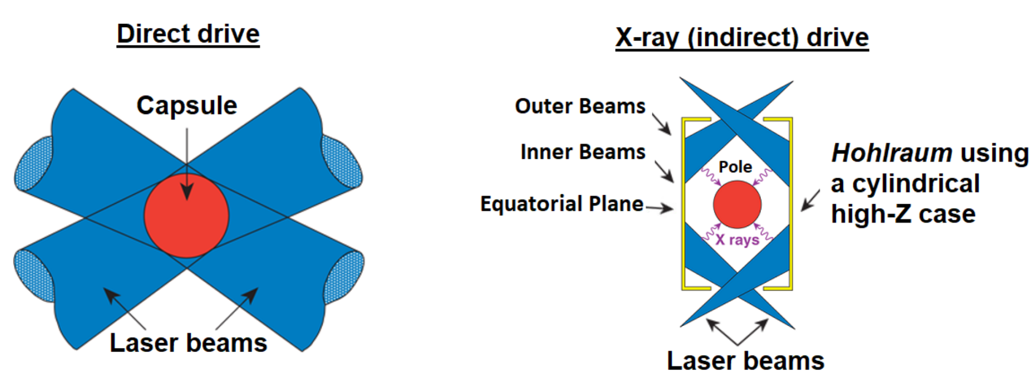

Figure 1: *The difference between the two main approaches to ICF, direct and indirect drive. The drawing on the right is a cross-section of a cylindrical hohlraum*

The cylindrical hohlraum is currently used at the National Ignition Facility (NIF) [2] at the Lawrence Livermore National Laboratory, which is the current largest ICF facility and is intended primarily for indirect drive. One potential flaw with this hohlraum design is that the fuel capsule implodes nonuniformly. At earlier phases of the implosions, the majority of the drive on the capsule is from the deposited laser energy spots. At later times, the majority of the drive is due to the heated hohlraum wall. During the implosion, material ablates from the hohlraum wall, and it becomes difficult for the inner beams to reach the equator of the hohlraum, reducing drive on the equatorial region of the capsule. The cylindrical hohlraum, however, can be "tuned," in which the specific pointings of the beams can be adjusted prior to the experiment, and/or the powers of the beams can be varied during the pulse (e.g., a laser pulse shape in which the powers of the inner beams are increased at later times) such that a greater uniformity can be achieved. However, tuning the beam powers to achieve uniform implosions is challenging to accomplish.

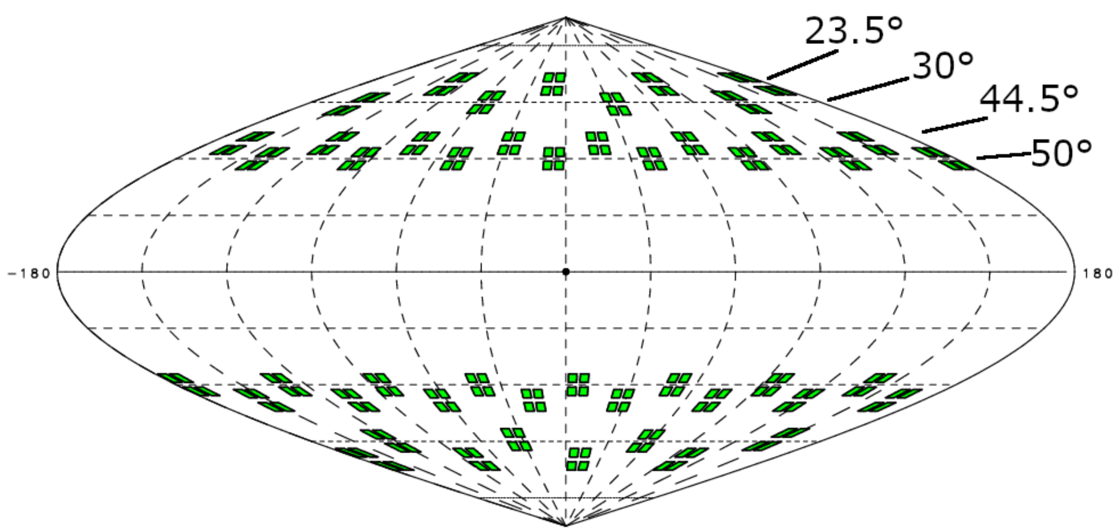

Figure 2: *Location of laser beam ports on the NIF target chamber*

In addition, direct drive is not a practical option with the current NIF target chamber design since the NIF beam ports are designed to perform predominantly indirect drive experiments with the cylindrical hohlraum. Figure 2 depicts the beam ports on the NIF, which are arranged in four rings at angles of 23.5°, 30.0°, 44.5°, and 50.0° from the vertical, and similarly for the lower hemisphere. The NIF contains 48 quads, which are groups of four beams. If the NIF beams are pointed at normal incidence to the fuel capsule for direct drive experiments, the poles of the capsule are overdriven as compared to the equatorial region. To perform direct drive experiments on the NIF, beams must be repointed towards the equator of the target. Some beams are repointed as much as 35° (from 50° to 85°) [3, 4], which can cause undesired levels of nonuniformity since beams that are repointed by a large angle may "miss" the target as the capsule compresses (energy in the beam refracts around the edge of the capsule without being significantly absorbed). The NIF target chamber is therefore not suited to provide uniform implosions during direct drive.

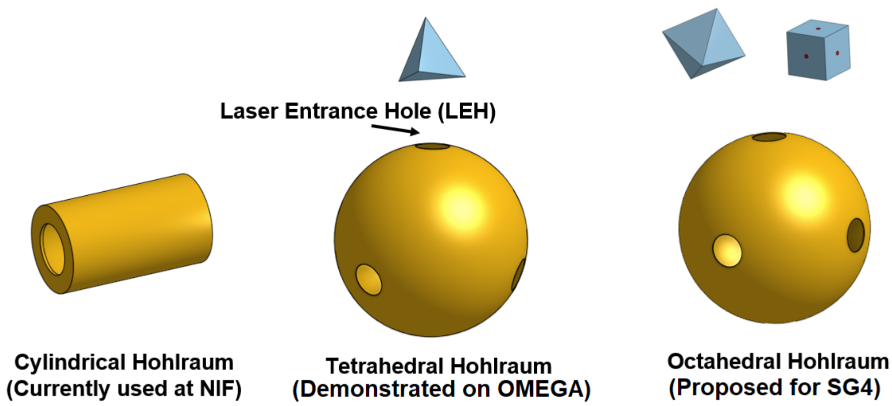

Figure 3: *Shown from left to right: Cylindrical, Tetrahedral, Octahedral Hohlraums*

The tetrahedral hohlraum was proposed to provide better uniformity for indirect drive [5, 6, 7]. As shown in Fig. 3 (middle), the tetrahedral hohlraum has four laser entrance holes located corresponding to the vertices of a tetrahedron. The tetrahedral hohlraum has been tested on the 60-beam OMEGA laser and has been shown to provide high levels of uniformity [8, 9].

Recently, octahedral hohlraums have been proposed as a more uniform alternative to the cylindrical hohlraum [10, 11, 12]. As shown in Fig. 3 (right), the octahedral hohlraum has six laser entrance holes corresponding to the centers of cube faces or the vertices of an octahedron. Due to the better geometric symmetry, the octahedral hohlraums should provide higher levels of uniformity during indirect drive as compared to the cylindrical and tetrahedral hohlraums. The NIF, however, does not match the cubic symmetry of the hohlraum and is not suited to drive it.

The SG4 Laser [13] is currently a concept in China and is planned to be a NIF-sized system (also with 48 quads) intended to drive the octahedral hohlraum. This work proposes amendments to the current SG4 target chamber design so that the SG4 laser can be used for direct drive in addition to indirect drive. Minor modifications are made to the current design to allow for high levels of uniformity when driving the octahedral hohlraum along with good levels of uniformity for direct drive. A new 3-D view-factor code, *LORE*, was created to model the capsule uniformity during indirect drive using spherical hohlraums. *LORE* predicts that the proposed target chamber achieves similar levels of uniformity as compared to the current design. In addition, the 2-D hydrodynamics code *SAGE* was used to find beam pointings which would produce good direct drive uniformity.

The Appendix proposes a hohlraum with 7 LEH's for experiments on the 60-beam OMEGA laser to study uniformity in spherical hohlraums. Five LEH's are arranged on the equator based on the vertices of a pentagon with 2 LEH's on the poles.

II Amended Design of SG4 Target Chamber

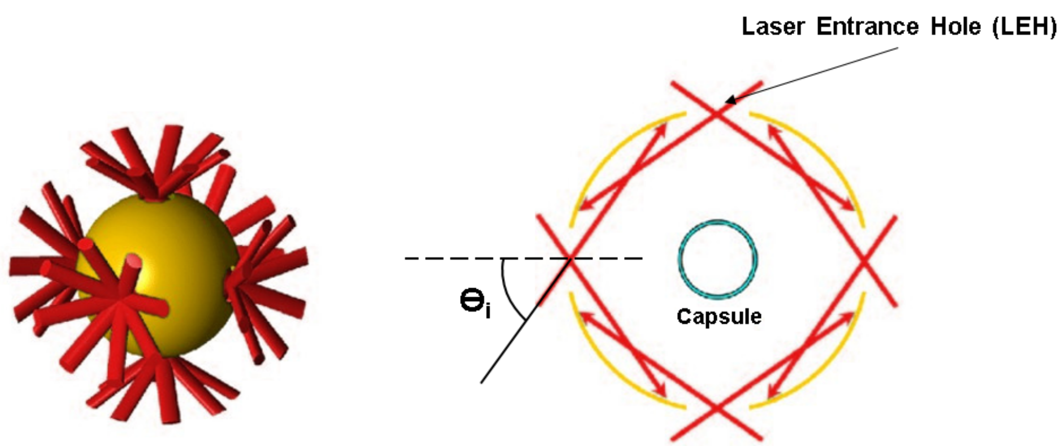

Figure 4: *3-D view of incident beams (left) and 2-D cross section of incident beams (right). From Ref. 10*

The beam arrangement envisaged for the SG4 laser to drive the octahedral hohlraum is shown in Fig. 4. Beams must enter this hohlraum at acceptable angles. Ideally, the angle of incidence θ_i ranges from 50° to 60° [10]. Beams entering at angles less than 50° have the risk of leaving through another LEH, crossing with other beams, or depositing energy onto the capsule. On the other hand, if the angle of incidence is greater than 60°, the beam may come too close to the edge of an LEH and ablate the gold [10]. This can cause unwanted plasma physics in which the beam deposits its energy into the plasma rather than the hohlraum wall.

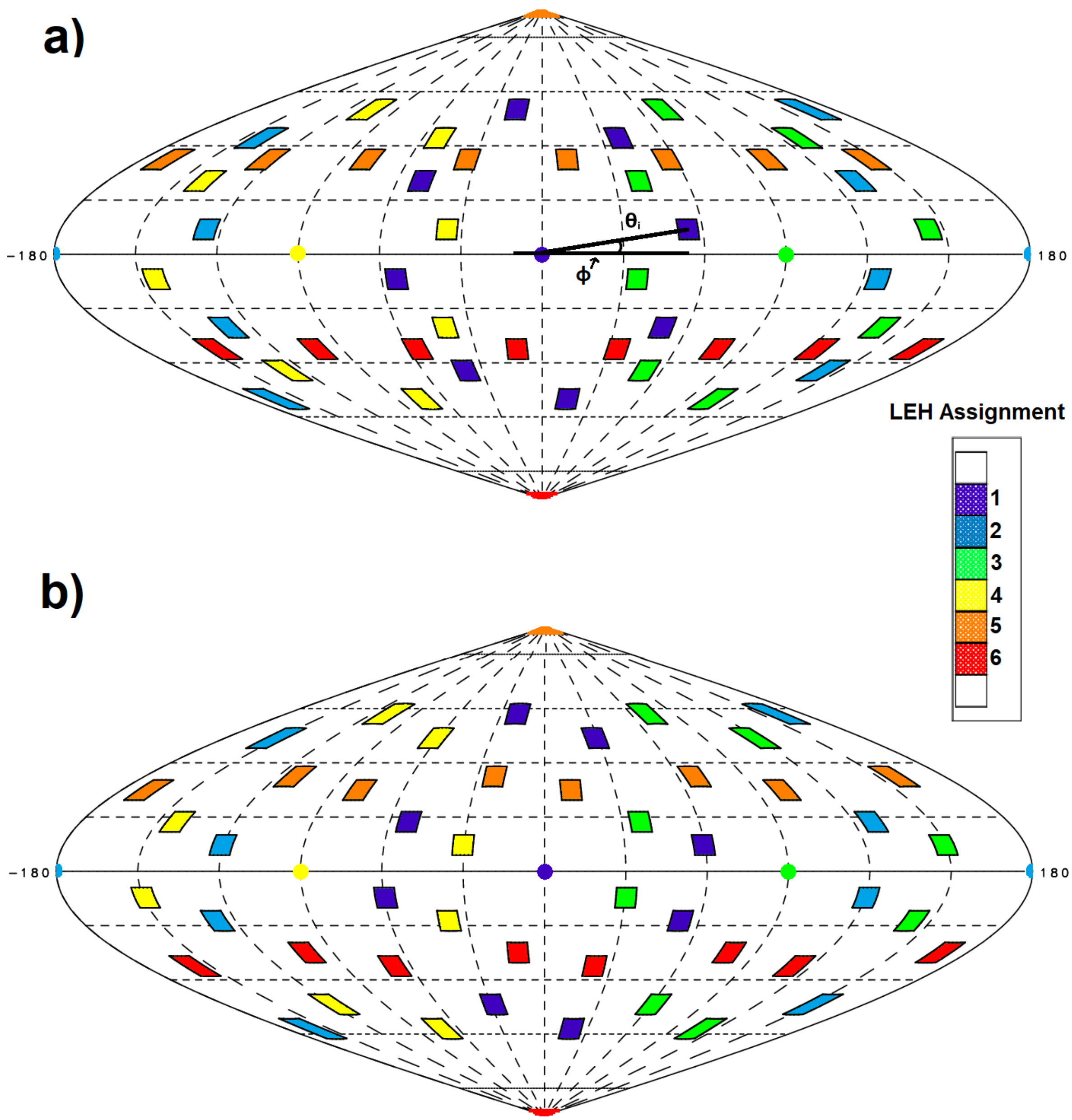

Figure 5: *Location of beam ports on the current target chamber (a) and the amended/proposed target chamber (b). The colored circles indicate the locations of the hohlraum LEH's (not drawn to scale)*

Figure 5 shows the location of beam ports on both the current and proposed target chambers. The colors of the beam ports correspond to the LEH through which the beam enters, with locations indicated by the colored circles (4 LEH's around the equator and 2 on the poles). The laser ports are configured in such a way that there are eight laser ports assigned to each LEH of the octahedral hohlraum (8 quads x 6 holes = 48 quads). Ports are placed on a "ring" which is θ_i degrees from the LEH, and ϕ denotes the angle of the beam on the ring. The current design, as shown in Fig. 5(a), sends all beams at an angle θ_i of $55°$ and uses $11.25°$ for ϕ to avoid overlapping laser spots [10, 11]. Although this target chamber is optimal for indirect drive with the octahedral hohlraum, the "clustering" of beam ports translates to an overall lower uniformity during direct drive. However, this design can be amended to be better suited for direct drive.

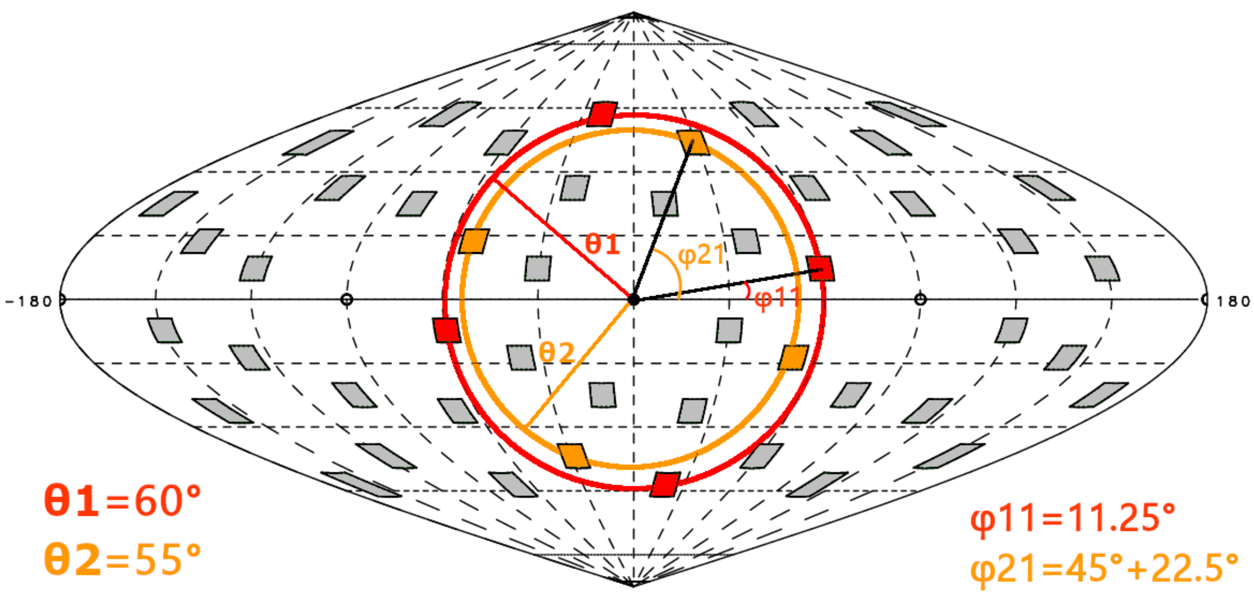

Figure 6: *Locations of odd beams (red) and even beams (orange) assigned to one LEH in the proposed design. The four beams of each group are spaced* $90°$ *in* ϕ

In the proposed design, as shown in Fig. 5(b) and Fig. 6, the θ and ϕ values for "odd" ports differ from the "even" ports in the group of eight. The odd half of the beams are sent at an angle of $60°$, and the even half at an angle of $55°$. The proposed chamber is still capable of driving the octahedral hohlraum as all the incident angles are within the acceptable range.

The odd ports are placed on a "ring" in which θ_1 is 60° from the center of the LEH (see Fig. 6). The ϕ values of the odd ports, ϕ_{1n}, are defined by:

$$\phi_{1n} = 11.25^\circ + 90.0^\circ * (n-1),\ n = 1-4 \tag{1}$$

Each even port is placed on a ring with a θ_2 value of 55° from the center of the LEH and the ϕ values are defined by:

$$\phi_{2n} = 45^\circ + 22.5^\circ + 90.0^\circ * (n-1),\ n = 1-4 \tag{2}$$

The laser ports on the proposed design are more evenly dispersed as compared with the current design, in which many beams are clustered together. This allows the amended chamber to provide good levels of uniformity during direct drive implosions, as later shown in Section V. The uneven spacing around the circles (the difference between 11.25° and 22.5°) is also to avoid ports associated with different LEH's from interfering.

III 3-D View-Factor Code *LORE*

The 3-D view-factor code *LORE* evaluates the capsule uniformity during indirect drive with a spherical hohlraum. *LORE* uses the same physics as is included in the code *Buttercup*, described in Ref. 6. *Buttercup* handles cylindrical and tetrahedral hohlraums, whereas *LORE* handles spherical hohlraums with any number of LEH's. While the description of *LORE* given here is focused on the octahedral hohlraum, the code can handle an arbitrary number of holes and beam ports.

III.1 Ray Trace Beams

LORE begins raytracing beams in the center of the entered LEH. The user specifies the LEH radius (r_{LEH}) and the beam cross sectional shape in the plane of the LEH (either circular or elliptical). The user also inputs the radius of the beam, r_o, which is typically $\frac{1}{2}r_{LEH}$. The beam cross section is then converted into a 2-D grid (shown in Fig. 7) of one million individual rays, each parallel to the beam direction and containing its own power.

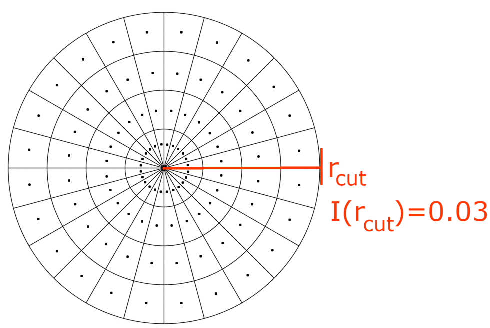

Figure 7: *2-D (r, θ_{ray}) grid of a circular beam cross section. Each grid cell contains one ray. Black circles indicate starting locations of rays. r_{cut} is the maximum distance r that rays are defined*

The power of each ray is determined by the area of its grid cell and the beam's intensity, $I(r)$, which is based on the distance r from the beam center and is assumed to be given by:

$$I(r) = I_o e^{-(\frac{r}{r_o})^n} \tag{3}$$

The constant, I_o, is determined from the total power in the beam such that the sum of all the ray powers equals the power of the beam. All the ray powers in all beams add up to P_{las}, the total power of the laser. Rays are first defined in (r, θ_{ray}) coordinates, but are later translated to Cartesian coordinates. r_o is the distance from the center to the $\frac{1}{e}$ intensity contour of the circular/elliptical cross section (for elliptical cross sections, r_o is based on the specific ray's angle of rotation θ_{ray}). The parameter, n, is taken to be around 8-12. A higher value for n signifies a greater "drop-off" in intensity for rays near the edge of the beam. In Fig. 7, r_{cut} is the maximum value of r for which rays are defined, and typically occurs when $e^{-(\frac{r}{ro})^n} = 0.03$ (a "cutoff" value).

Using vector equations, *LORE* then finds the intersection of each ray with the hohlraum wall. At that intersection, *LORE* calculates the fraction of energy deposited, $A(\theta)$, with θ being the angle of incidence on the hohlraum wall. An assumption can be made that $A(\theta) = 1$ (beams deposit all their energy at the first intersection) as large hohlraums have shown high levels of absorption [1]. *LORE* can, however, include a bounce, in which the fraction of energy deposited is based on the formula:

$$A(\theta) = 1 - \exp(-b * \cos^r(\theta)) \tag{4}$$

As in Ref. 7, the parameters b and r are taken to be 3 and 1, respectively. Thus, the absorption of one intersection is around 80% for $\theta_i = [55, 60]^\circ$. After finding the first intersection, the bounce is calculated by reflecting the ray and then determining a second intersection. According to *LORE*, when either the current design or the proposed design is used to drive the octahedral hohlraum, no beam energy is directly deposited onto the capsule, and no energy is lost to the LEH's after two intersections.

LORE defines points on the hohlraum wall according to a cube grid. Each of the six faces of a cube contains 100x100 grid points, each of which defines a direction that corresponds to a location on the hohlraum wall (making 60,000 points on the hohlraum wall). Quantities such as deposited laser energy and effective radiation temperature are defined at each point on the cube grid. After an intersection between a ray and the hohlraum wall is found, the deposited laser energy is distributed amongst the nearest four grid points using bilinear interpolation. (The cube grid was used in Ref. 14 to describe a nonuniform ice layer in a cryogenic ICF capsule and illustrated in Fig. 12 of Ref. 15)

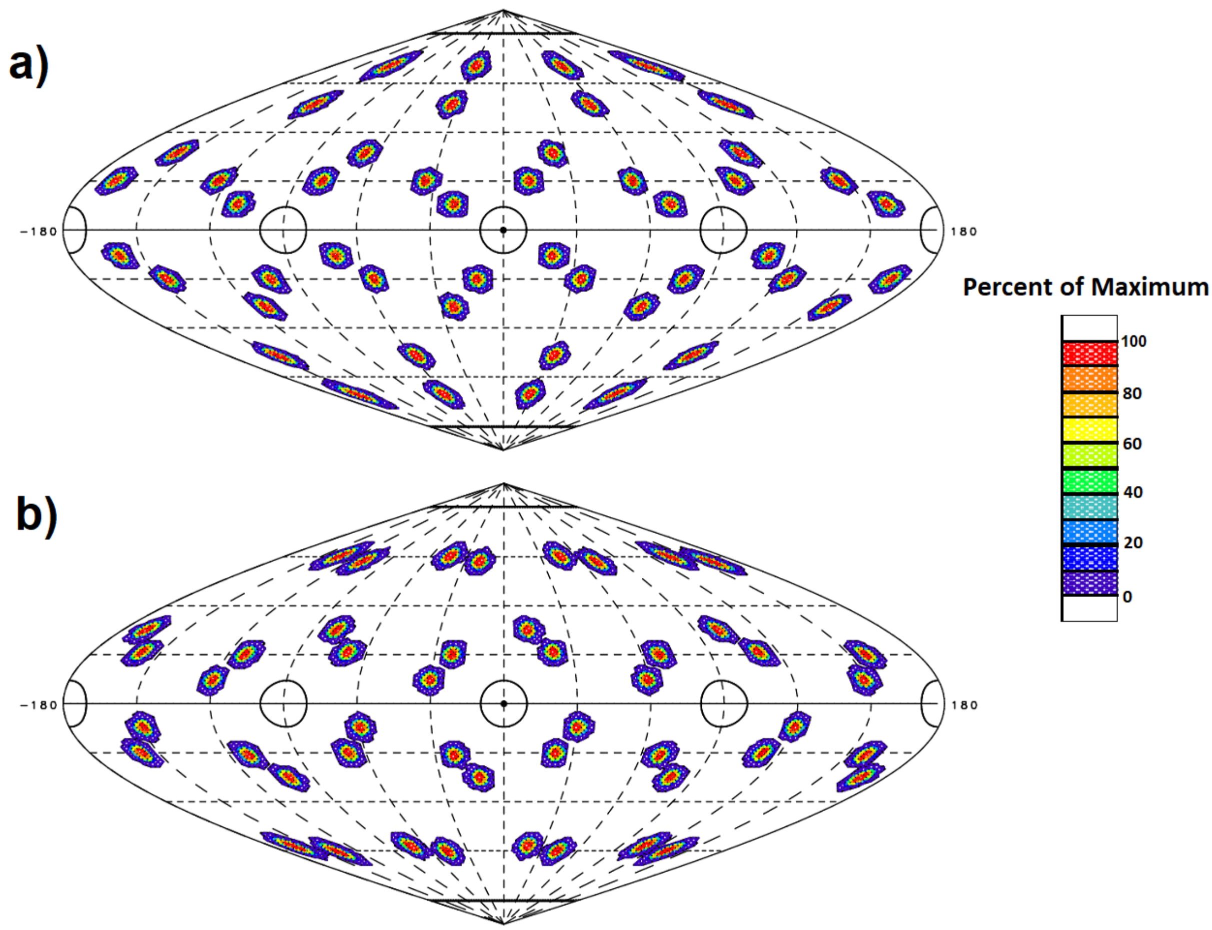

Figure 8: *Deposited laser energy per unit area on an octahedral hohlraum for the current target chamber design (a) and the proposed design (b). The LEH's are indicated with outlines*

Figure 8 depicts the deposited laser energy per unit area on an octahedral hohlraum for just one intersection ($A(\theta) = 1$). In both target chamber designs, there is no overlap of deposited energy. In addition, for both designs, the locations of deposited energy are spread fairly uniformly around the hohlraum wall. Thus, there are only minor differences between the two chamber designs when driving the octahedral hohlraum.

III.2 Determine Effective Radiation Temperature

After tracing all the beams, *LORE* determines a background, or equilibrium radiation temperature T_r by assuming an equilibrium Planckian radiation field in the hohlraum. The temperature T_r is calculated by balancing power entering the radiation field with power lost due to the LEH's and absorption by the hohlraum wall and capsule [Equation (2) of Ref. 6].

$$P_{las}\eta_L = \sigma T_r^4 (NA_h + B_w A_w + B_c A_c) \tag{5}$$

P_{las} is the total absorbed power of the laser (simulations for the proposed design use 410 TW as P_{las}) and A_h, A_w, A_c are the areas of the LEH's, hohlraum wall, and capsule, respectively. σ is the Stefan-Boltzmann constant, so σT_r^4 is the intensity of the background radiation in power/unit area. η_L is the efficiency of the conversion of laser energy to x-ray energy and is taken to be 0.8 [11]. B_w and B_c are the fractions of the background radiation energy absorbed by the hohlraum wall and the capsule, respectively. B_c is taken to be large (0.9). B_w is equal to $1 - \alpha_w$, where α_w is the wall albedo, or the fraction of radiation energy reflected by the hohlraum wall. α_w generally increases as the hohlraum walls heats up. Thus, wall albedo is a time-dependent variable. N is the number of LEH's.

Next, *LORE* calculates the effective radiation temperature T_e at every point on the wall, which is determined by the background radiation that is reflected by the hohlraum wall plus the fraction of absorbed laser power that is converted to radiation at that point (in Eq. (6), I_L is the absorbed laser power per unit area at that point):

$$\sigma T_e^4 = \alpha_w \sigma T_r^4 + \eta_L I_L \tag{6}$$

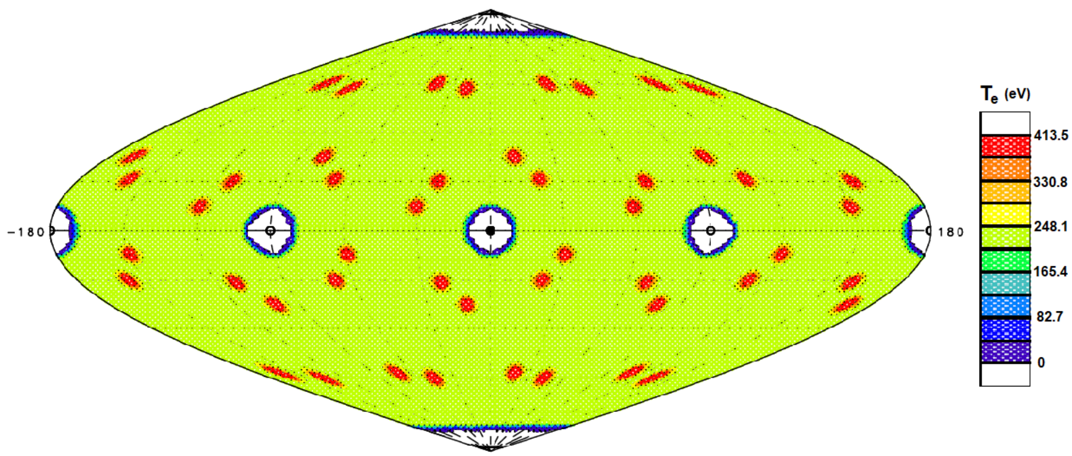

Figure 9: *Contour plot of effective radiation temperature T_e of the hohlraum wall at an albedo α_w of 0.85. $T_r \sim 244$ eV*

Figure 9 depicts the effective radiation temperature at all points on the hohlraum wall for the same parameters as were used for Fig. 8(b). The white circles, which represent LEH's, emit no radiation. It should be noted that the most intense (red) spots correspond to the laser spots on Fig. 8(b) and emit more radiation flux than the rest of the hohlraum wall, but this difference is less substantial at a higher albedo α_w. In addition, the associated area of these spots is only a small fraction of the hohlraum wall.

The parameters used for Fig. 9 are based on the dimensions given in Section IV for a typical octahedral hohlraum and an albedo of 0.85. T_r, the background radiation temperature determined from Eq. (5), is approximately 244 eV. A background radiation temperature of 270 to 300 eV is generally desired for ignition. Ignition occurs when helium nuclei produced by fusion redeposit their energy in the compressed fuel, causing more fusion to occur.

III.3 Integrate Radiation Flux

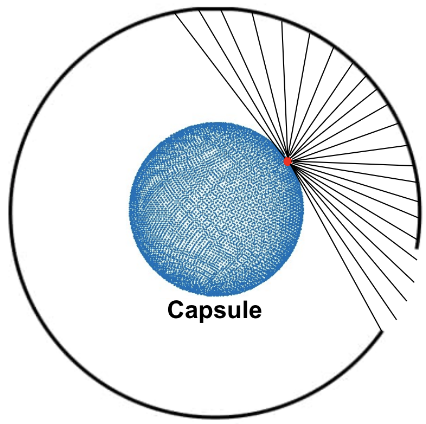

Figure 10: *Schematic of the algorithm used by LORE to determine the radiation flux at each point on the capsule. LORE scans over multiple points on the capsule, looks over a number of directions, and accumulates spectral brightness to determine the radiation flux. [Based on Fig. 4 of Ref. 6]*

After determining the effective radiation temperature at all points on the hohlraum wall, *LORE* scans over multiple points on the capsule. For each point, as indicated in Fig. 10, *LORE* integrates the spectral brightness over various angles of θ (direction altitude) from 0 to $\frac{\pi}{2}$ and ϕ (direction azimuth) from 0 to 2π to determine the radiation intensity at that point:

$$I = \int_0^{\frac{\pi}{2}} \int_0^{2\pi} B(\theta,\phi)\cos(\theta)\sin(\theta)d\phi d\theta \tag{7}$$

The brightness, $B(\theta,\phi)$, is $\sigma T_e^4/\pi$, or the power emitted per unit area per unit solid angle from the hohlraum wall. The $\sin(\theta)$ accounts for the solid angle and the $\cos(\theta)$ considers the angle between the surface element of the capsule and the incoming ray [6]. These integrals typically involve scanning 60,000 points on the capsule and for each point, looking over $\sim$ 100,000 directions.

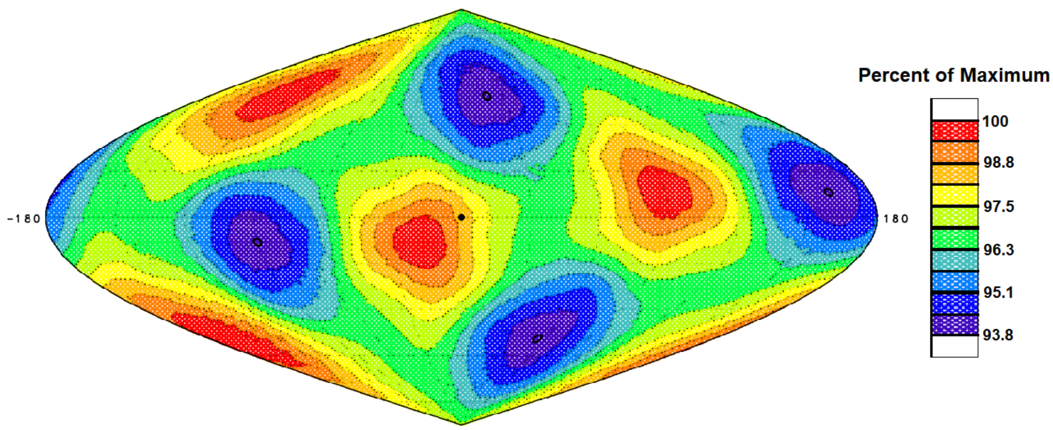

(a) Tetrahedral, Albedo=0.85, RMS $\sim$ 1.44%

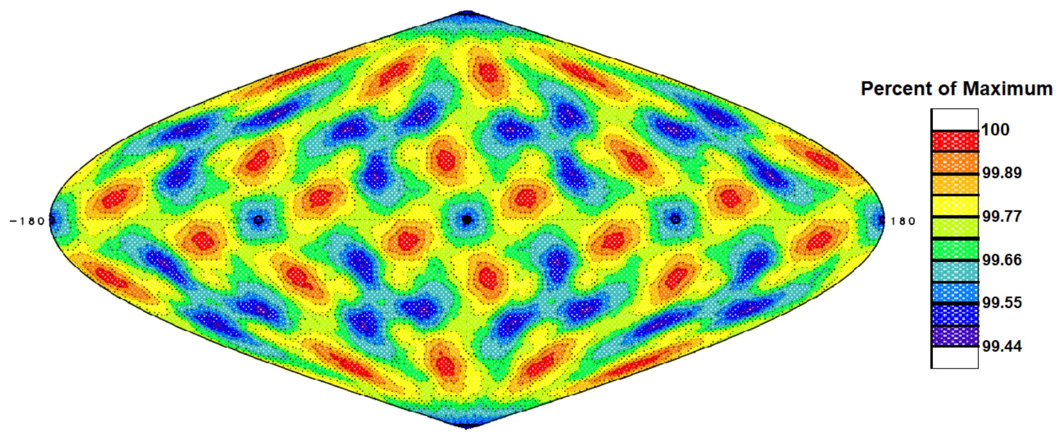

(b) Octahedral, Albedo=0.85, RMS $\sim$ 0.10%

Figure 11: *Capsule uniformity contour plots for tetrahedral (a) and octahedral (b) hohlraums at albedos α_w of 0.85*

Figure 11 depicts the uniformity of radiation flux on the capsule at an albedo α_w of 0.85 produced by *LORE* simulations comparing tetrahedral and octahedral hohlraums. The octahedral hohlraum produces lower levels of nonuniformity than the tetrahedral hohlraum (0.10% compared to 1.44%; note the difference in scales)

The octahedral hohlraum simulation, shown in Fig. 11(b), uses the parameters outlined in Section IV, different from the parameters used in the tetrahedral hohlraum simulation (based on Ref. 7). If the capsule radius, hohlraum radius, and laser pulse were the same as those used in the tetrahedral hohlraum simulation, however, *LORE* predicts that the octahedral hohlraum would provide a nonuniformity rms of 0.15%, still significantly lower than 1.44%.

IV Results from *LORE* for Indirect Drive

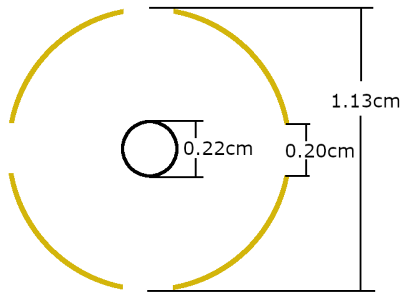

Figure 12: *Dimensions of octahedral hohlraum used in this paper*

Figure 12 depicts the the octahedral hohlraum dimensions used for the *LORE* simulations, unless otherwise noted. These dimensions are based on the "golden" octahedral hohlraum of Ref. 10. $R_{capsule} = 0.11$ cm, $R_{LEH} = 0.1$ cm, $R_{hohlraum} = 0.5654$ cm ($R_{hohlraum}$ is taken to be $5.14 * R_{capsule}$, which is referred to as the "golden ratio" for octahedral hohlraums [12]).

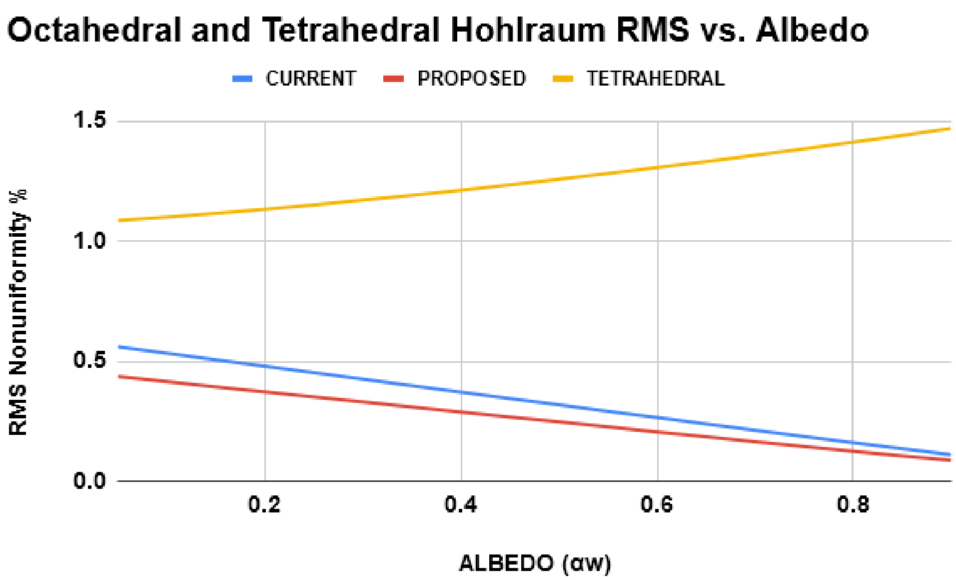

Figure 13: *RMS nonuniformity for octahedral (blue-current, red-proposed) and tetrahedral (yellow) hohlraums for various albedo α_w*

Figure 13 shows a comparison of capsule uniformity between the current and proposed designs for the octahedral hohlraum. The results for the tetrahedral hohlraum are included as a benchmark, using parameters corresponding to the optimized "Scale 1.2" tetrahedral hohlraum of Fig. 1 of Ref. 7 ($R_{capsule} = 275\ \mu$m, $R_{LEH} = 350\ \mu$m, $R_{hohlraum} = 1400\ \mu$m $= 5.09{*}R_{capsule}$). Different from Ref. 7, the beams are assumed to propagate with parallel rays (as described in Sec. III.1) and pass through the center of each LEH with a circular cross section in the plane of the LEH. Interestingly, the hohlraum-to-capsule ratio used in Ref. 7 is close to the "golden ratio" of Ref. 12.

According to Fig. 13, the octahedral hohlraum provides notably better uniformity than the tetrahedral hohlraum and the x-ray nonuniformity is less than 1% over all values of albedo. At lower albedos, the deposition pattern of the laser spots plays a dominant role in the capsule uniformity. At higher albedos, the majority of the capsule drive is from the heated hohlraum wall, and the uniformity is determined predominantly by the geometric symmetry of the hohlraum. The octahedral/cubic symmetry clearly provides better uniformity than the tetrahedral symmetry.

The proposed design provides higher levels of uniformity than the current design, but only by a slight margin. This is primarily due to the difference in the location of deposited laser energy (Fig. 8). This shows that the proposed target chamber achieves similar results to the current chamber when driving the octahedral hohlraum.

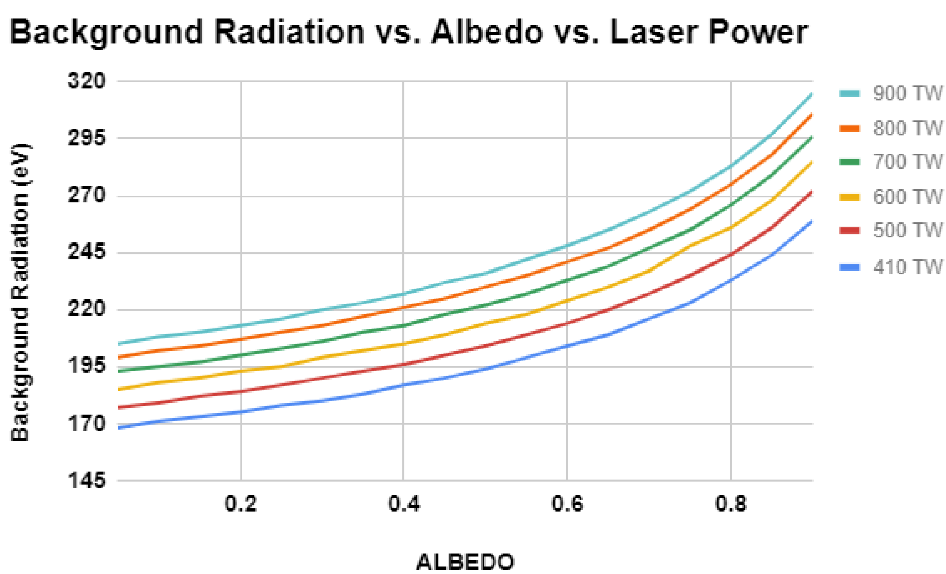

Figure 14: *Background radiation temperature T_r as a function of albedo α_w for various laser powers, for a hohlraum-to-capsule ratio of 5.14*

Figure 14 shows the octahedral hohlraum background radiation temperature T_r as a function of albedo α_w for multiple laser powers. Since T_r is proportional to the $\frac{1}{4}$th power of the laser power, significant increases in the laser power result in small changes in the background temperature. With the hohlraum-to-capsule radius ratio of 5.14, a large laser power, above the upper limit of the NIF peak power of around 500 terawatts, is required in order to achieve the 270-300 eV required for ignition. A smaller hohlraum radius is therefore desirable to increase the background radiation temperature. Therefore, another topic of interest is how the hohlraum-to-capsule-radius ratio affects the uniformity.

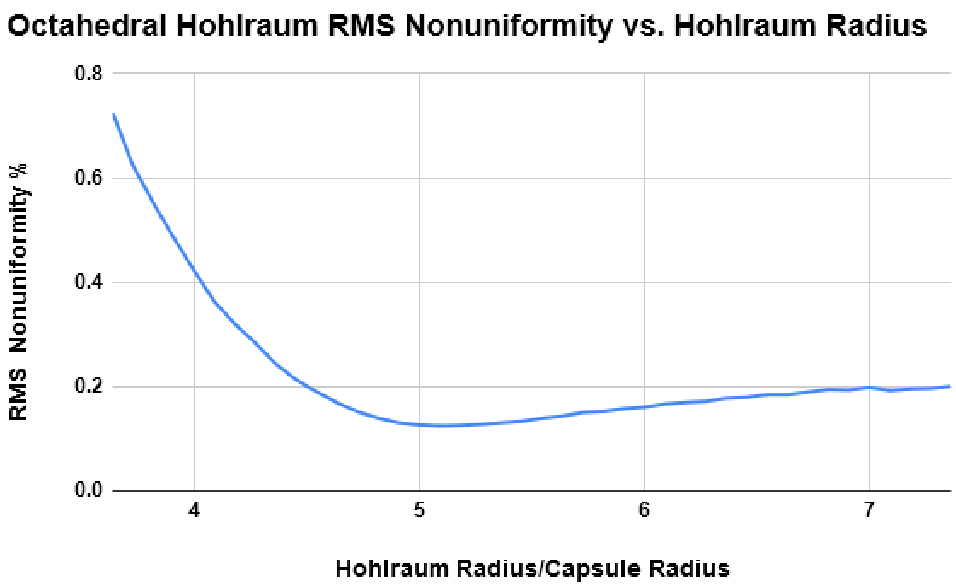

Figure 15: *RMS nonuniformity for octahedral hohlraums as a function of the ratio of hohlraum-to-capsule radius at an albedo α_w of 0.8. The capsule radius (0.11 cm) and LEH radius (0.1 cm) are fixed*

This is illustrated in the *LORE* simulations of Fig. 15. Here the capsule and LEH radius are kept the same, and the hohlraum radius is varied (note the albedo α_w is 0.8, not 0.85). A hohlraum-to-capsule ratio of around 5.1 presents a local minimum of $\sim$0.12% in RMS nonuniformity. This is consistent with the "golden ratio" of 5.14 found in Ref. 12. A smaller ratio will provide a greater background radiation temperature, but at the expense of uniformity, as nonuniformity steeply increases as this ratio decreases.

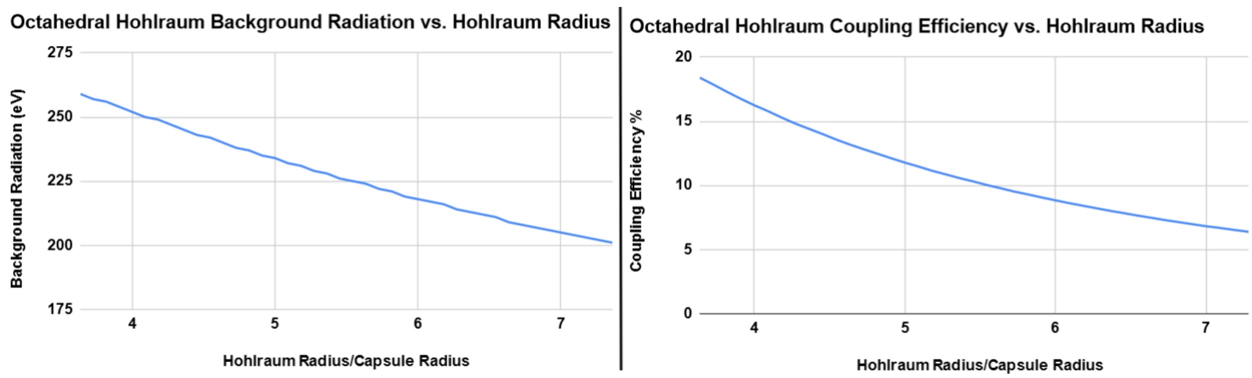

Figure 16: *Background radiation temperature (left) and coupling efficiency (right) for octahedral hohlraums for various values of hohlraum-to-capsule-radius ratio at an albedo of 0.8 and fixed capsule and LEH radii (0.11 cm and 0.1 cm, respectively). The laser power is 410 TW*

As shown in Fig. 16, as the hohlraum radius increases for a fixed capsule radius, the background radiation temperature and the coupling efficiency steadily decrease. The coupling efficiency is the fraction of the incident laser power absorbed on the capsule. These results guide the choice of a hohlraum-to-capsule-radius ratio that will accommodate this tradeoff. Different octahedral hohlraum shapes are being considered to increase the radiation temperature and coupling efficiency [16].

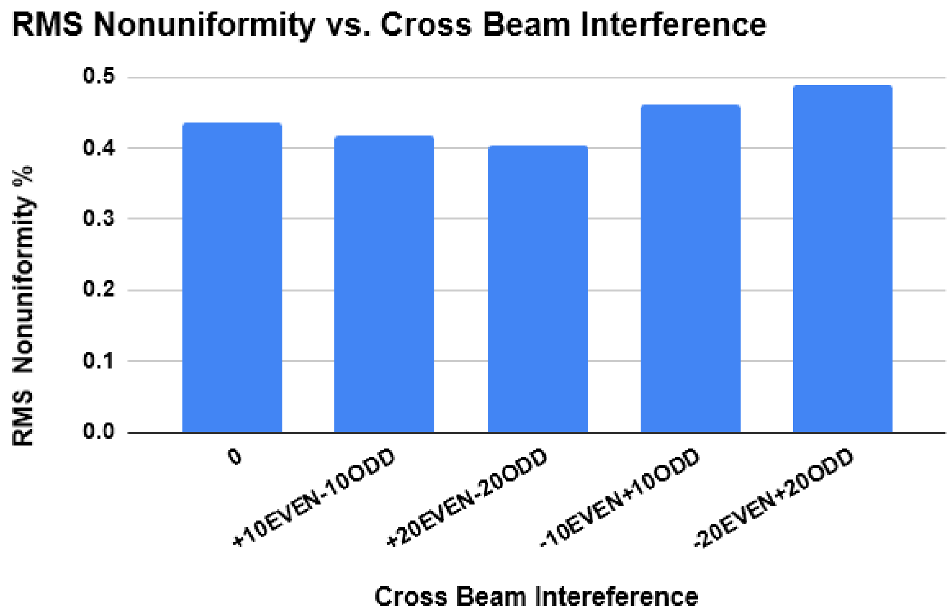

Figure 17: *RMS nonuniformity for an octahedral hohlraum with various scenarios of cross beam energy transfer. (+10EVEN-10ODD signifies a 10% power increase to even beams and -10% in odd beams). Albedo* α_w*=0.05*

Another factor to take into consideration is the effect of cross beam energy transfer (CBET) [17] on the uniformity on the capsule. CBET is the phenomenon in which, when two beams cross, energy from one beam can transfer to the other (this occurs when beams pass through the LEH's). According to Ref. 10, this does not occur when all beams have the same angle of incidence because all beams are essentially equivalent. CBET is unlikely to be significant for the minor differences ($\theta_i = 55°$ vs. $\theta_i = 60°$).

Figure 17 demonstrates this for various hypothetical energy shifts. The fractions of power for the odd (θ_i =60°) and even (θ_i =55°) beams are altered by $\pm$ 10-20%. The albedo used in Fig. 17 is 0.05. At low albedos, the background radiation contributes little to the drive on the capsule and the beam spots are more significant. Thus, an albedo of 0.05 was used as it demonstrates the biggest effect on nonuniformity. Even with drastic changes to the beam powers, however, there are no significant effects on uniformity. At higher albedos, the effect of CBET on uniformity is lessened, as the heated hohlraum wall dominates the drive on the capsule.

V Results from the 2-D Hydrodynamics Code *SAGE* for Direct Drive

As shown from *LORE* simulations, the proposed target chamber is capable of producing similar levels of uniformity for indirect drive of an octahedral hohlraum as compared to the current design (with beams entering at 55°). The main difference between the two designs, however, is that the proposed chamber allows for the option of direct drive experiments.

The following *SAGE* simulations assume a spatial profile given by Eq. (3) with a beam radius r_o of 0.11 cm and a supergaussian index n of 3.0 in the best-focus plane.

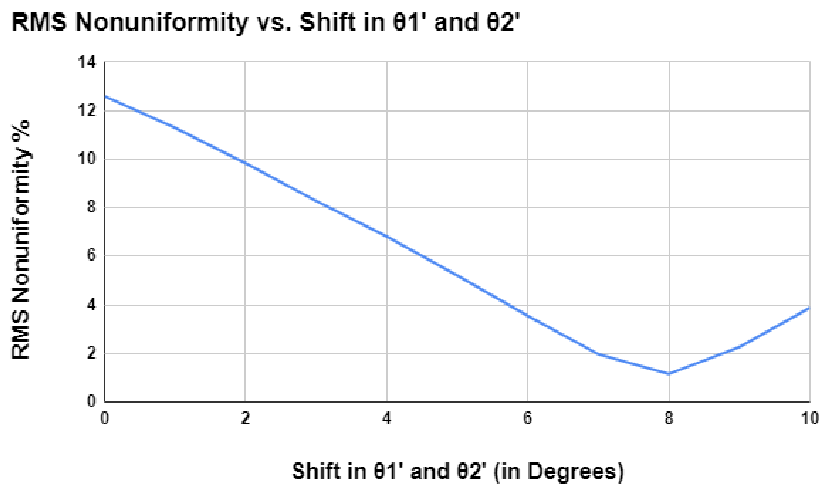

Figure 18: *RMS nonuniformity on the capsule as a function of beam pointing shifts* $\Delta\theta_1$ *and* $\Delta\theta_2$ *(assumed equal here) for direct-drive SAGE simulations using the proposed target chamber design*

Figure 18 depicts the nonuniformity of the cumulative deposited laser energy on the capsule as a function of beam repointing angles based on *SAGE* simulation results. In these runs, the beams are not pointed at normal incidence; instead, they are slightly shifted and aimed towards a different location on the capsule. Each beam is repointed by:

$$\theta_j' = \theta_j + \Delta\theta_j,\ \ j = [1,2] \tag{8}$$

$$\phi_{jn}' = \phi_{jn} + \Delta\phi_j,\ \ j = [1,2] \text{ and } n = 1-4 \tag{9}$$

θ_1 (odd) and θ_2 (even) represent the theta value of a laser port with respect to its associated

LEH (60° for odd ports, 55° for even ports). A value of ∼8.0° for both $\Delta\theta_1$ (odd beams) and $\Delta\theta_2$ (even beams) presents a local minimum of around 1.15% RMS nonuniformity. In the series of runs in Fig. 18, the values of ϕ'_{1n} and ϕ'_{2n} are unchanged ($\Delta\phi_1 = \Delta\phi_2 = 0$).

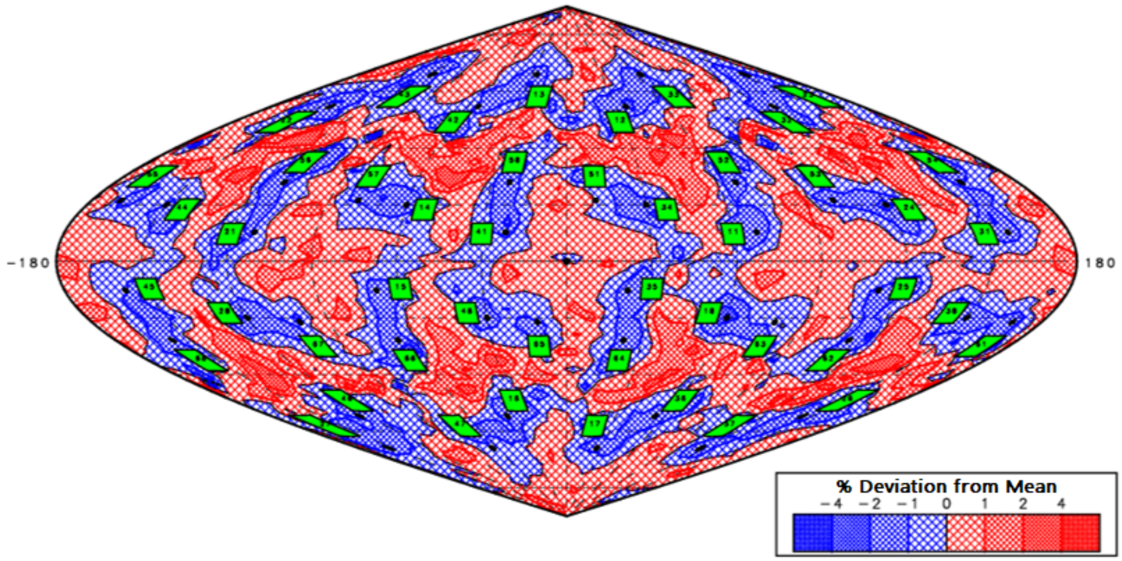

Figure 19: *Target uniformity of deposited laser energy for direct drive using beam repointings optimized for the assumed spatial profile. RMS∼1.06%. Green boxes represent locations of the laser ports, and black dots depict locations on the capsule to which the beams are pointed*

After further optimization of beam repointings including nonzero $\Delta\phi_1$ and $\Delta\phi_2$, Fig. 19 depicts the uniformity of the cumulative deposited laser energy on the capsule. The green boxes represent the locations of the laser ports, and the small black dots (excluding the one in the center) depict the locations on the capsule to which the beams are pointed. For the purpose of testing the performance of the target chamber configuration, each quad is considered to be one beam. Without altering the specific pointings of each of the four beams in a quad, the optimum design shown in Fig. 19 gives a nonuniformity rms of 1.06%.

In Fig. 19, the odd beams are pointed at $\theta'_1 = \theta_1 + 8.5°$, with θ_1 = 60°. The theta values of the even beams are repointed by 7.1°, thus $\theta'_2 = \theta_2 + 7.1°$, with $\theta_2 = 55°$. In addition, the ϕ value of each beam is shifted by -0.2° ($\Delta\phi_1 = \Delta\phi_2 = -0.2°$).

The *SAGE* simulation parameters used in Figs. 18 and 19 are of a 4 mm diameter CH capsule imploded with 1.1 MJ (typical for a NIF experiment). These specifications are comparable to what would be expected for a direct drive target experiment on the SG4 laser at a comparable energy.

With further optimization, separate repointing of the four beams of a quad, and using a different spatial profile (e.g., with a larger beam radius r_o), a nonuniformity rms of $<$1% can be expected. As opposed to the direct drive experiments on the NIF, in which the beams are repointed by as much as 35°, the beams in the proposed design are repointed by less than 9°. The proposed design is therefore well suited for direct drive experiments.

VI Conclusion

This work proposes minor modifications to the current SG4 target chamber design to allow for direct drive in addition to indirect drive. A view-factor code, *LORE*, was built to calculate the capsule uniformity for spherical hohlraums. The proposed target chamber, as shown by *LORE* simulations, is capable of achieving high levels of capsule uniformity when driving the recently proposed octahedral hohlraum. Without making adjustments to the pointings of the different groups of laser beams and without using different laser pulse shapes for different groups of beams, the uniformity for indirect drive ranges from 0.44% at earlier times in the implosion to 0.11% during later stages, both comfortably less than the 1% generally thought to be required. Further, simulation results from the 2-D hydrodynamics code *SAGE* demonstrate that, with slight repointing of the 48 quads, the proposed target chamber can provide good levels of uniformity ($\sim$1%) for direct drive experiments. Further optimization of the 192 beam pointings and spatial profiles can be expected to achieve results of higher uniformity.

Acknowledgements

I must give my sincerest thanks to my advisor and program director, Dr. R. Stephen Craxton, for all of his assistance. Dr. Craxton was always eager and willing to devote countless hours when providing me with help throughout the entire program. I would also like to thank Ms. Jean Steve for helping organize this eight-week high school program. Finally, I would like to thank Eugene Kowaluk for taking incredible pictures throughout the program and my fellow interns for providing a comfortable work environment.

Appendix (7-hole hohlraum)

The recent interest in spherical hohlraums based around octahedral designs has been extended by Ref. 18, which analyzed symmetry properties for values of n, the number of LEH's, up to 12, including a design for $n = 7$ of "a pentagon at the equator with two points at the poles." This Appendix proposes a hohlraum design with 7 holes to be used for experiments on the 60-beam OMEGA laser, which may be used to explore the performance of spherical hohlraums. Simulations of the Scale 1.2 tetrahedral hohlraum experiments carried out on OMEGA predicted low levels of nonuniformity (less than 1% during most of the laser pulse) [7]. Simulations from *LORE* of the 7-hole design predict a nonuniformity ranging from 1.10% at early stages to 0.6% at final stages.

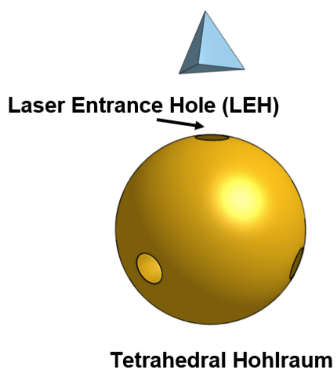

Figure A1: *Shown from left to right: Tetrahedral, PEPR hohlraums*

As shown in Fig. A1 (right), the locations of the LEH's on the 7-hole hohlraum are based on the centers of the faces of a pentagonal prism (this paper will refer to the 7-hole hohlraum as the "*PEPR*" hohlraum).

The following *LORE* simulations of the tetrahedral hohlraum use the same hohlraum dimensions as Section IV (based on Ref. 7) and the parameters of the OMEGA laser. The parameters used for the *PEPR* hohlraum are the same as those used for the tetrahedral hohlraum, except for the number of LEH's and locations of LEH's (the LEH radii are kept the same to avoid laser clearance issues).

LEH	(θ,ϕ)	Beams
1	(90°, 36°)	31, 10, 66, 24, 15, 35, 67, 14, 21, 50
2	(90°, 108°)	11, 13, 65, 32, 47, 18, 42, 23, 57, 62
3	(90°, 180°)	68, 58, 48, 59, 60, 53, 49, 69, 51, 54
4	(90°, 252°)	55, 52, 28, 40, 36, 63, 16, 44, 38, 29
5	(90°, 324°)	26, 20, 33, 41, 27, 37, 34, 43, 39, 12
6	(0°, 0°)	22, 56, 61, 46, 17
7	(180°, 0°)	30, 25, 45, 64, 19

Figure A2: *LEH assignments used in LORE simulations for a PEPR hohlraum. Numbers in the third column indicate OMEGA beam names*

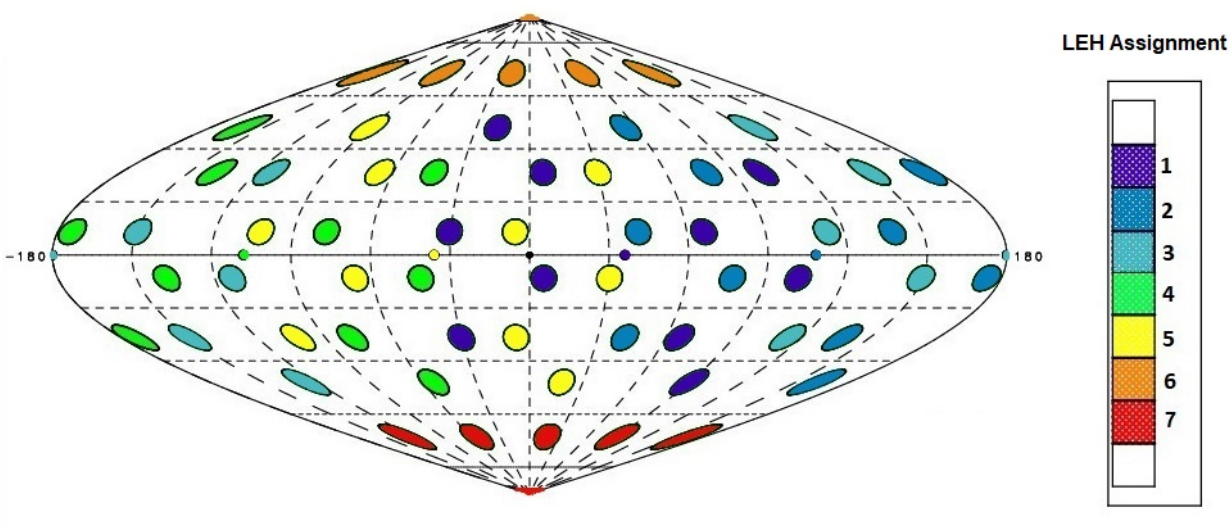

Figure A3: *LEH assignments used in LORE simulations for a PEPR hohlraum. Colors of beam ports represent LEH assignment. The small colored circles indicate the LEH locations*

Figures A2 and A3 depict one viable set of beam assignments of the OMEGA laser for driving the *PEPR* hohlraum. The angle of incidence θ_i ranges from 21.4° (beams sent to the two LEH's on the poles) to 69.7°. For comparison, θ_i ranges from 23.2° to 58.8° for the tetrahedral hohlraum [7].

When driving the tetrahedral hohlraum, each of the 60 beams must be sent through the nearest LEH due to the angle of separation between the 4 LEH's. For the *PEPR* hohlraum, however, there are options for which LEH each beam may be sent through. As an example, the beam located at (θ=21.4°, ϕ = 54°) may enter either LEH 1 (with θ_i=69.7°) or LEH 6 (with θ_i=21.4°). Therefore, Figs. A2 and A3 are not the only plausible set of beam pointings; additional pointings may be devised for a variety of experiments.

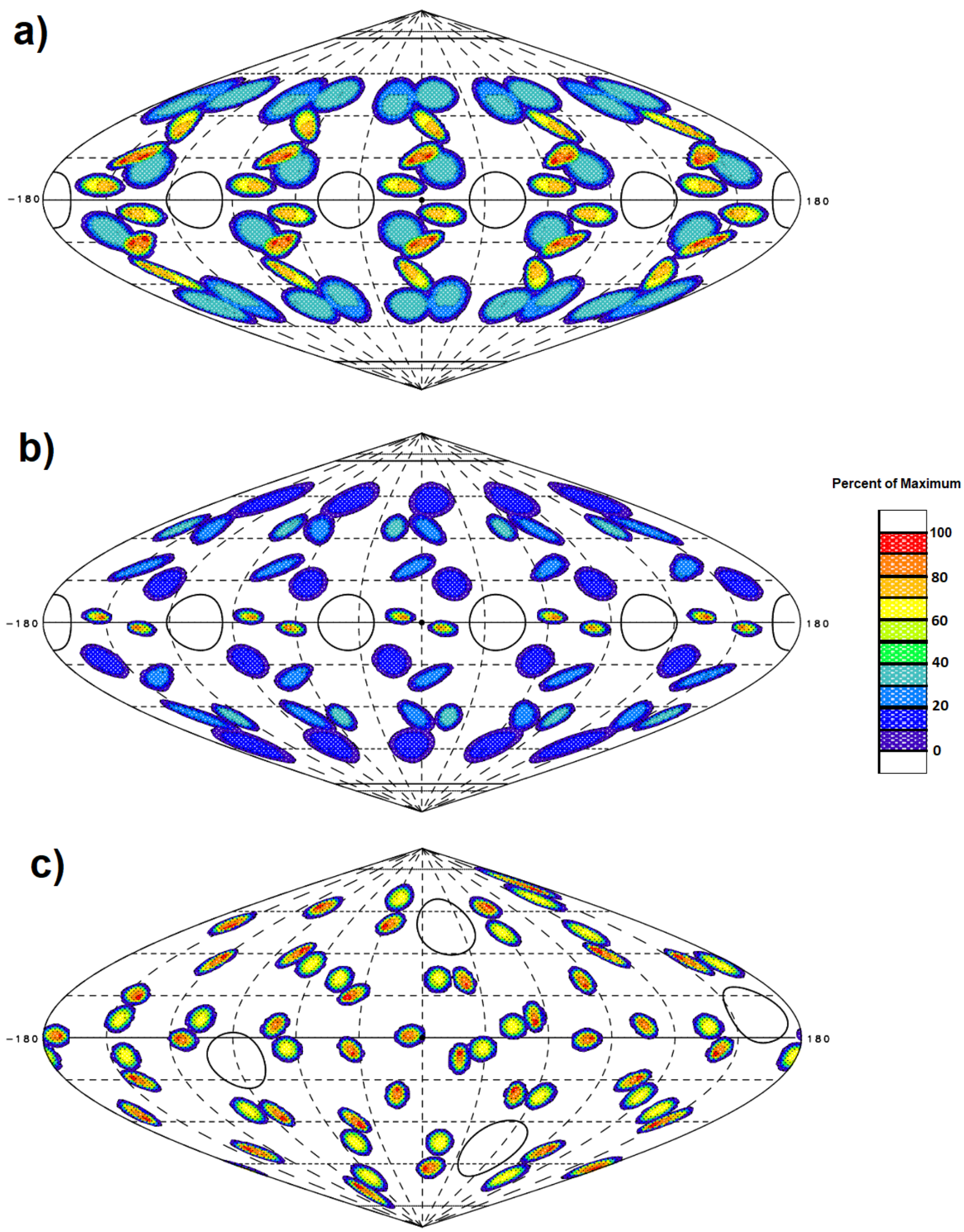

Figure A4: *Deposited laser energy per unit area on a PEPR hohlraum without beam repointing (a), with repointing (b), and on a tetrahedral hohlraum (c). The LEH's are indicated with outlines*

The beams may also be repointed by changing their best focus point. In Sec. IV, the tetrahedral hohlraum simulations assumed the use of phase plates, so the beams were modeled as parallel rays with a circular cross section in the plane of the LEH. The beams also travelled through the center of each LEH. For the following *PEPR* and tetrahedral hohlraum simulations, *LORE* uses the parameters of the 60-beam OMEGA laser, the beams are modeled as circular cones with an $f/6$ focus, and the best focus points are specified as user input. As for the experiments of Refs. 8 and 9, phase plates are not used.

Figures A4(a) and A4(b) both represent deposited laser energy (for just one intersection) on a PEPR hohlraum using the beam assignments shown in Figs. A2 and A3. For Fig. A4(a), the best focus point of each beam is in the center of the entered LEH, whereas Fig. A4(b) shifts the best focus points to improve capsule uniformity (see Fig. A9), increase clearance with the capsule (see Fig. A6), and maintain at least a 50 μm clearance when entering the LEH's (see Fig. A7). In addition, after repointing the beams, the locations of deposited energy are well clear of the LEH's and there are fewer overlaps.

Figure A4(c) shows the deposited laser energy on a tetrahedral hohlraum for just one intersection ($A(\theta) = 1$). The parameters used for the tetrahedral hohlraum are based on the tetrahedral hohlraum experiments modeled in Ref. 7, but the beam pointings have been optimized to improve uniformity. The tetrahedral hohlraum simulations will be used as benchmarks for the *PEPR* hohlraum.

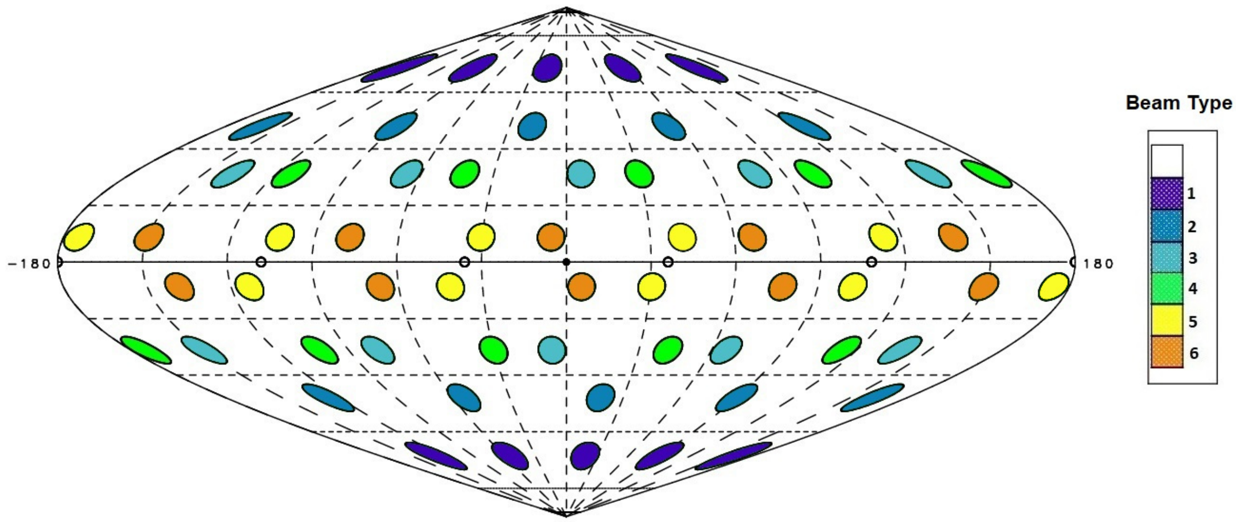

Figure A5: *Six types of beams entering the PEPR hohlraum. Based on the LEH assignments of Fig. A3*

Figure A5 depicts the six "types" of beams used to drive the *PEPR* hohlraum. The beam type is based on the angle at which the incident beam enters the LEH (in contrast to Fig. A3, where the colors indicate LEH assignments). For example, the beams which enter the polar LEH's are all considered to be the same type of beam. All the beams of a specific beam type have a similar travel path within the hohlraum and are repointed similarly for the current optimized pointings. The symmetries for each equatorial LEH and both polar LEH's are therefore maintained after the beams are repointed.

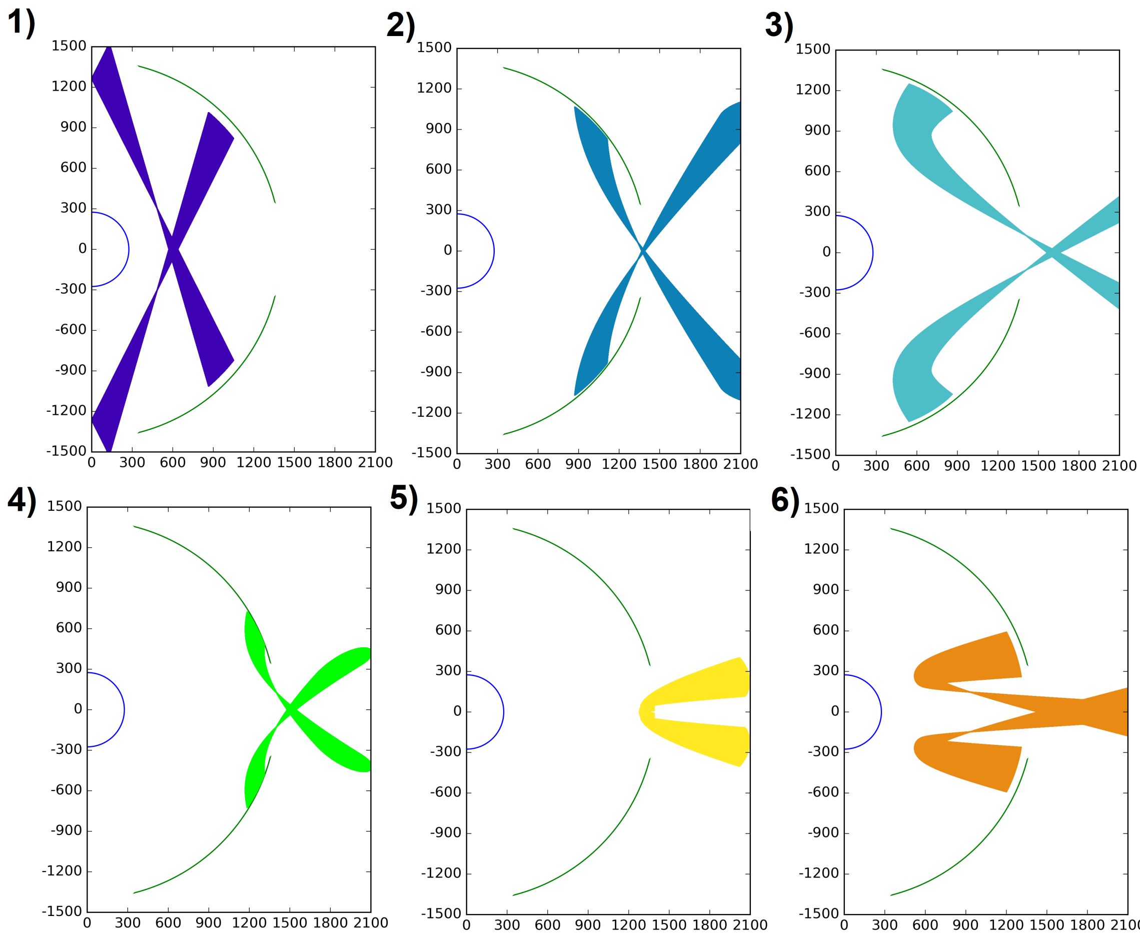

Figure A6: *2-D view of the six types of beams entering the PEPR hohlraum (using optimized pointings). The z-value is plotted on the vertical axis, with* $\sqrt{x^2+y^2}$ *on the horizontal axis. Units are in microns*

Figure A6 depicts 2-D views of the six types of beams entering the *PEPR* hohlraum with optimized pointings. The color of each beam type follows the color code of Fig. A5. The blue inner semi-circle depicts the capsule, while the larger green semi-circle depicts the hohlraum wall. The segments of the hohlraum wall that are not drawn represent the LEH's. Since the equatorial LEH's are equivalent under rotations about the vertical axis, only one equatorial LEH is shown.

For each 2-D view, $\sqrt{x^2+y^2}$ is plotted on the horizontal axis, enabling one to check the clearance with the capsule and to see the θ of where the laser beam strikes the wall. The repointed beams offer more clearance with the capsule. Beam type 1 is shifted away from the capsule, and the best focus point is positioned near the capsule to provide greater clearance. The ϕ values are not shown in Fig. A6. For example, for beam type 6, no rays exit through an LEH; the spots are close to the equator but clear of the LEH's (see the approximately circular spots in Fig. A4(b) $\sim$ 20° from the equator), hitting the wall with ϕ different by $\sim 25°$.

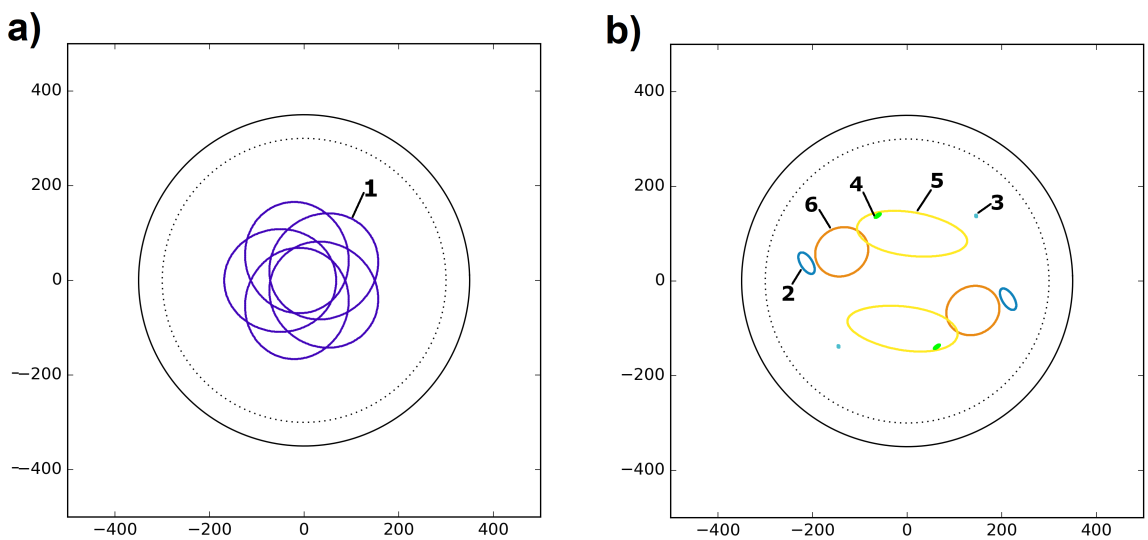

Figure A7: *2-D cross section view of the optimized pointed beams entering the PEPR hohlraum polar LEH's (a) and equatorial LEH's (b) in the plane of the LEH. The dotted circle depicts a 50 μm clearance. The beam cross sections are labeled and colored according to type as defined in Fig. A5. Units are in microns*

Figure A7 represents the incident beam cross section in the plane of the LEH for both the polar LEH's (a) and the equatorial LEH's (b). The colors of the beam cross sections in Fig. A7 correspond to the six beam types. The current optimized pointings of the beams also satisfy the clearance with the LEH. The dotted circle is drawn to demonstrate that the beams clear the LEH's with at least a 50 μm clearance, based on Ref. 6.

Some of the beam cross sections in the equatorial LEH (Fig. A7(b)) appear as small dots, since the best focus point is close to the LEH and *LORE* does not model the diffraction of the beams, which would widen the spots. In reality, the spot size would be about 50 μm in diameter at best focus [7]. Regardless, there would still be greater than 50 μm clearance with the actual spot sizes.

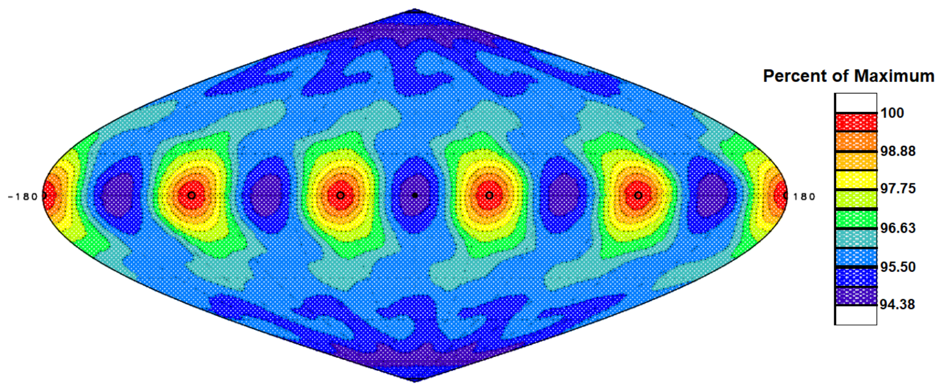

(a) *PEPR*, Albedo=0.05, RMS ∼ 1.10%

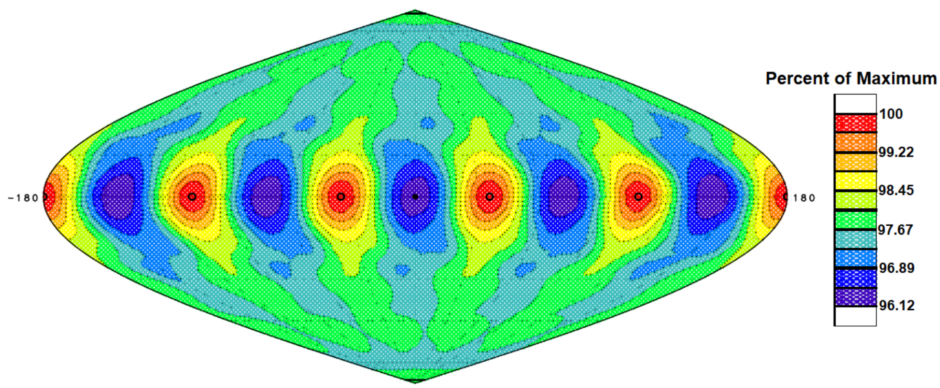

(b) *PEPR*, Albedo=0.50, RMS ∼ 0.67%

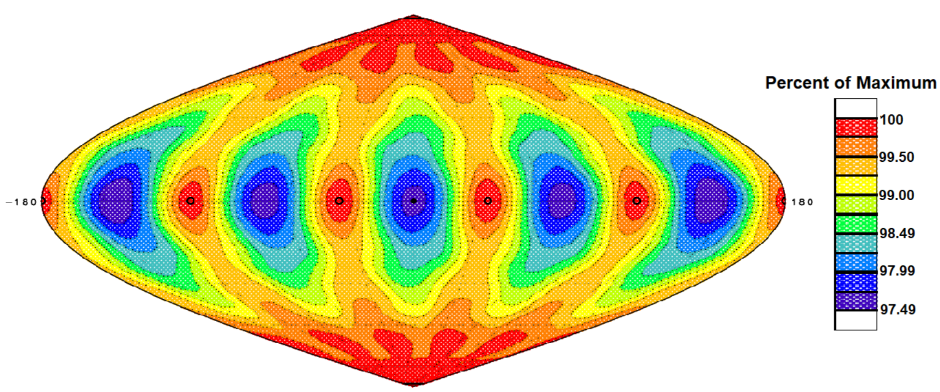

(c) *PEPR*, Albedo=0.85, RMS ∼ 0.60%

Figure A8: *Capsule uniformity contour plots for the optimized PEPR hohlraum at albedos α_w of 0.05 (a), 0.50 (b), and 0.85 (c). (Note the difference in scales)*

Figure A8 depicts the capsule uniformity when driving a *PEPR* hohlraum with optimized beam pointings at albedos α_w of 0.05, 0.50, and 0.85 produced by *LORE* simulations. At lower levels of albedo, the laser spots dominate, and since the locations of deposited laser energy are more "clumped" around the equator than around the poles (Fig. A4(b)), the equatorial region of the capsule receives slightly more drive. However, at higher values of albedo, the heated hohlraum wall provides the dominant contribution to the drive. Due to the two LEH's on the poles being spaced further from other LEH's than the five equatorial LEH's, the poles of the capsule receive greater drive.

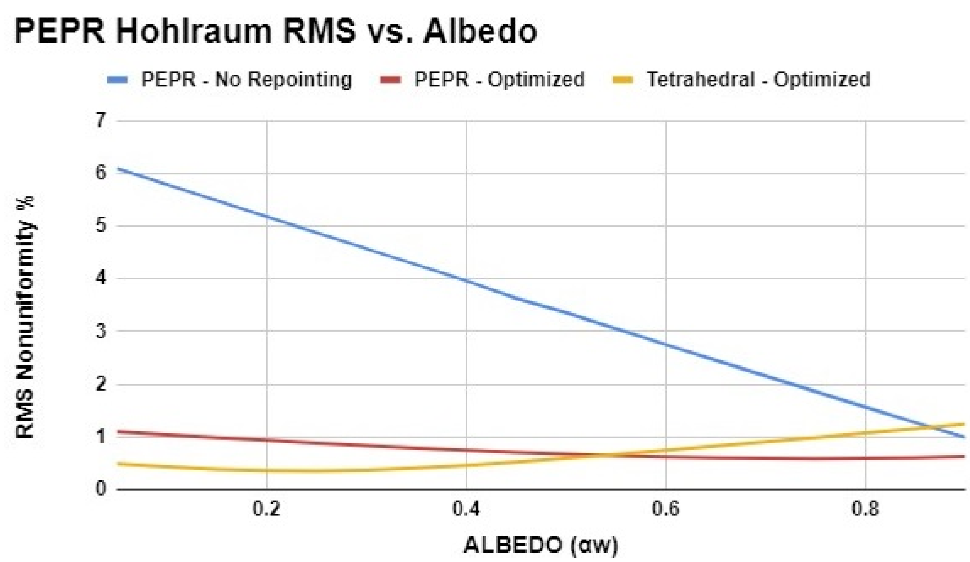

Figure A9: *RMS nonuniformity for unoptimized (blue) and optimized (red) PEPR hohlraums and tetrahedral hohlraums (yellow) for various albedo* α_w*. The tetrahedral curve uses optimized beam pointings and is different from the curve in Fig. 13*

Figure A9 shows a comparison of capsule uniformity between the tetrahedral and *PEPR* hohlraums (with and without repointing). Without repointing, there are significantly greater nonuniformities for the *PEPR* hohlraum, as the locations of deposited laser energy are not as uniformly dispersed (compare Figs. A4(a) and A4(b)). With the optimized pointings, however, the uniformity is improved at all values of albedo. The nonuniformity is reduced by a factor of 5 to 6 (6.10% to 1.10%) at an early time (albedo = 0.05), and at later times (albedo > 0.8) by about a factor of 2.

At lower values of albedo, the tetrahedral hohlraum provides better uniformity than the optimized *PEPR* hohlraum because the locations of deposited laser energy on the tetrahedral hohlraum are more evenly spread out (demonstrated in Fig. A4). At albedos greater than 0.5, however, the capsule nonuniformity is lower for the *PEPR* hohlraum, with the nonuniformity consistently around 0.6%.

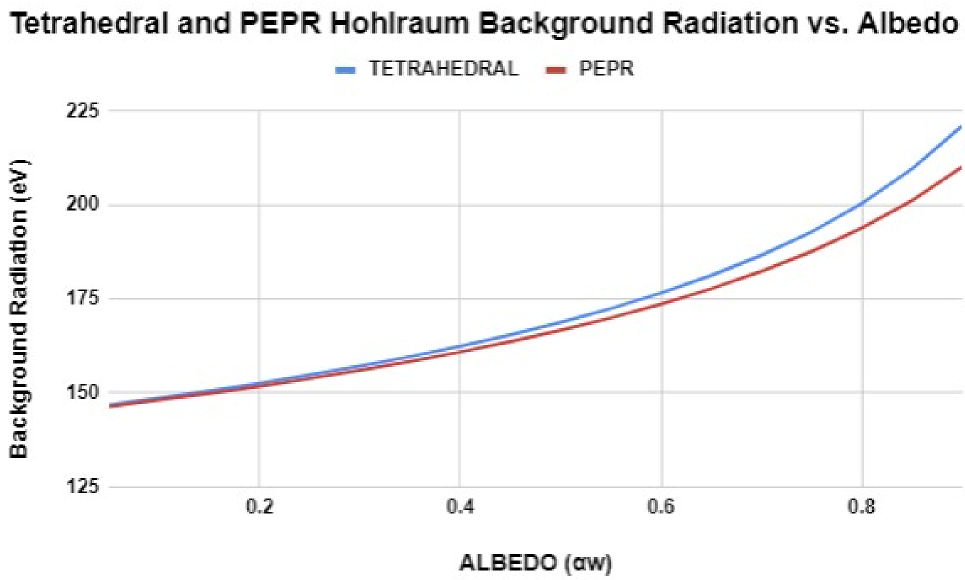

Figure A10: *Background radiation temperature T_r as a function of albedo α_w for tetrahedral (blue) and PEPR (red) hohlraums*

Figure A10 depicts the background radiation temperature T_r for tetrahedral and *PEPR* hohlraums as a function of albedo α_w. The total power of the 60-beam OMEGA laser P_{las} is taken to be 18 TW, approximately the peak power of the "PS22" laser pulse shape used to drive the tetrahedral hohlraums of Refs. 8 and 9. Due to the presence of three more LEH's, the *PEPR* hohlraum provides a lower T_r as compared to the tetrahedral hohlraum. Reducing the hohlraum radius somewhat (with the LEH radius fixed) to increase T_r would be plausible since the deposited laser energy is clear of the LEH's (as shown in Fig. A4).

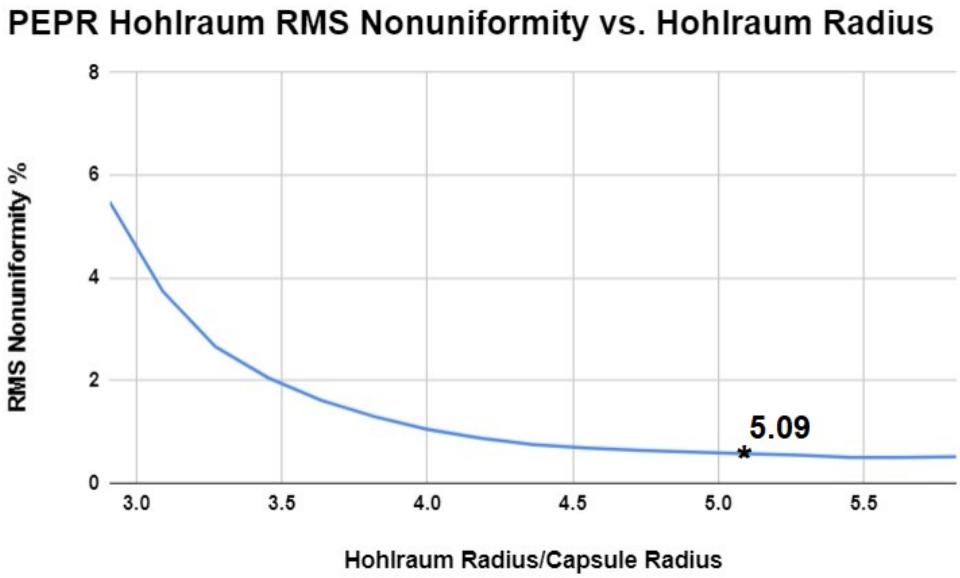

Figure A11: *RMS nonuniformity for PEPR hohlraums as a function of the ratio of hohlraum-to-capsule radius at an albedo α_w of 0.8. The capsule radius and LEH radius are fixed. The asterisk indicates the ratio for the standard PEPR and tetrahedral hohlraums used in this paper*

Figure A11 depicts the capsule nonuniformity while the hohlraum radius is varied (the capsule and LEH radii are kept the same). Each simulation used beam pointings that are similar to those optimized for a case-to-capsule ratio of 5.09. For different ratios, the beams are repointed in the same direction, but the distance shifted is based on the hohlraum radius. For example, each type 1 beam is repointed by 1200 μm for a standard *PEPR* hohlraum, but is repointed by 1.2*1200 μm for a case-to-capsule ratio of 1.2*5.09.

As opposed to the octahedral hohlraum, for which a hohlraum-to-capsule ratio of around 5.1 presents a local minimum, there does not appear to be a "golden ratio" for *PEPR* hohlraums. The RMS nonuniformity consistently decreases as the hohlraum-to-capsule ratio increases. As an example of the tradeoff between uniformity and radiation temperature, a hohlraum-to-capsule ratio of 4.35 would give a nonuniformity of 0.88% and increase T_r to 202 eV, a little higher than the 200 eV shown in Fig. A10 for the tetrahedral hohlraum. Since the beam pointings were initially optimized for a case-to-capsule ratio of 5.09, Fig. A11 is likely an overestimate of the nonuniformity that can be achieved at different ratios. Nevertheless, Fig. A11 gives a good indication of the tradeoff.

A possible method to improve capsule uniformity while minimally decreasing the background radiation temperature is to increase the size of the LEH's on the poles, as the regions near the poles of the capsule receive greater drive at higher albedos.

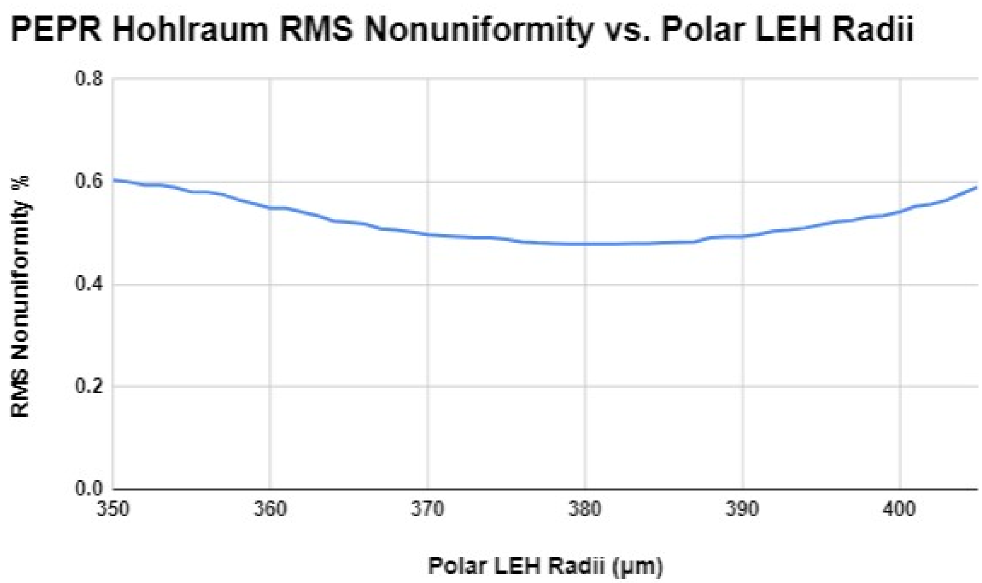

Figure A12: *RMS nonuniformity for PEPR hohlraums as a function of polar LEH radii at an albedo α_w of 0.85. The equatorial LEH radii are kept the same (350 μm)*

Various radii of polar LEH's are tested in Fig. A12, while the radii of the equatorial LEH's remain at 350 μm. At an albedo α_w of 0.85, a relative minimum for RMS nonuniformity of 0.48% occurs at a polar LEH radius of 380 μm, a minor improvement over the value of 0.60% found for equal LEH radii in Figs. A8(c) and A9. The background radiation temperature T_r is approximately 200 eV, compared to 201 eV for a standard *PEPR* hohlraum with equal size LEH's.

The simulations to create Fig. A12 used a higher resolution to reduce the "steps" in the curve which resulted from the way effective radiation temperature is defined in the vicinity of the LEH's. Each cube grid face contains 200x200 grid points, creating four times more points on the hohlraum wall than the 100x100 grid points used in the rest of the simulations in this paper (see Section III.1). The results with increased resolution are consistent with the rest of the paper and only deviated slightly (a difference of $\sim$ 0.05% in the RMS values) compared to the "standard resolution."

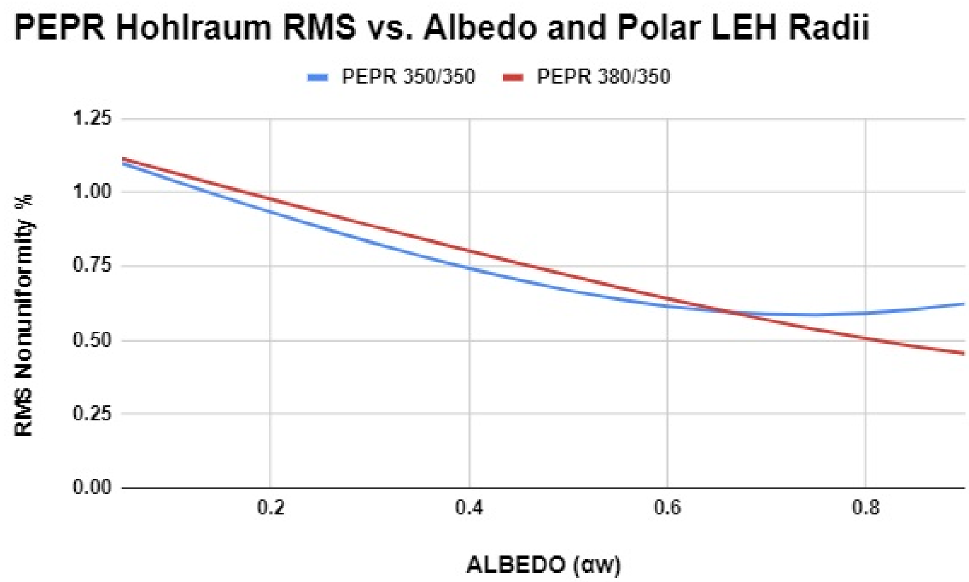

Figure A13: *RMS nonuniformity for the standard PEPR hohlraum (blue) and a PEPR hohlraum with polar LEH radii of 380 μm (red) as a function of albedo α_w. Both hohlraums use optimized beam pointings. The equatorial LEH radii are kept the same (350 μm). The standard PEPR curve is the same as that in Fig. A9*

Another point of consideration for *PEPR* hohlraums with increased polar LEH radii is the dependence of their uniformity on albedo. In Fig. A13, results for increasing the radii of the polar LEH's to 380 μm are compared with results for a standard *PEPR* hohlraum. The radii of the equatorial LEH's remain the same (350 μm), and the beam repointings are unaltered.

The *PEPR* hohlraum with increased polar LEH radii produces slightly higher nonuniformities compared to the standard *PEPR* hohlraum at low values of albedo. However, lower nonuniformities are achieved at all albedo values greater than 0.7. This is due to the poles being underdriven at low albedo values but overdriven at high albedos (Fig. A8). Thus, to obtain minimum overall nonuniformity, the radii of the polar LEH's may need to be greater than those of the equatorial LEH's, depending on the hohlraum and capsule dynamics.

References

[1] J. D. Lindl. "Development of the indirect-drive approach to inertial confinement fusion and the target physics basis for ignition and gain". In: *Physics of Plasmas* 2.11 (1995), pp. 3933–4024. DOI: 10.1063/1.871025. eprint: https://doi.org/10.1063/1.871025. URL: https://doi.org/10.1063/1.871025.

[2] C. A. Haynam et al. "National Ignition Facility laser performance status". In: *Appl. Opt.* 46.16 (2007), pp. 3276–3303. DOI: 10.1364/AO.46.003276.

[3] P. B. Radha et al. "Direct drive: Simulations and results from the National Ignition Facility". In: *Physics of Plasmas* 23.5 (2016), p. 056305. DOI: 10.1063/1.4946023. eprint: https://doi.org/10.1063/1.4946023. URL: https://doi.org/10.1063/1.4946023.

[4] T. J. B. Collins et al. "A polar-drive-ignition design for the National Ignition Facility". In: *Physics of Plasmas* 19.5 (2012), p. 056308. DOI: 10.1063/1.3693969. eprint: https://doi.org/10.1063/1.3693969. URL: https://doi.org/10.1063/1.3693969.

[5] D. W. Phillion and S. M. Pollaine. "Dynamical compensation of irradiation nonuniformities in a spherical hohlraum illuminated with tetrahedral symmetry by laser beams". In: *Physics of Plasmas* 1.9 (1994), pp. 2963–2975. DOI: 10.1063/1.870537. eprint: https://doi.org/10.1063/1.870537. URL: https://doi.org/10.1063/1.870537.

[6] J. D. Schnittman and R. S. Craxton. "Indirect-drive radiation uniformity in tetrahedral hohlraums". In: *Physics of Plasmas* 3.10 (1996), pp. 3786–3797. DOI: 10.1063/1.871511. eprint: https://doi.org/10.1063/1.871511. URL: https://doi.org/10.1063/1.871511.

[7] J. D. Schnittman and R. S. Craxton. "Three-dimensional modeling of capsule implosions in OMEGA tetrahedral hohlraums". In: *Physics of Plasmas* 7.7 (2000), pp. 2964–2977. DOI: 10.1063/1.874148. eprint: https://doi.org/10.1063/1.874148. URL: https://doi.org/10.1063/1.874148.

[8] J. M. Wallace et al. "Inertial Confinement Fusion with Tetrahedral Hohlraums at OMEGA". In: *Phys. Rev. Lett.* 82 (1999), pp. 3807–3810. DOI: 10.1103/PhysRevLett.82.3807. URL: https://link.aps.org/doi/10.1103/PhysRevLett.82.3807.

[9] G. R. Bennett et al. "Moderate-convergence inertial confinement fusion implosions in tetrahedral hohlraums at Omega". In: *Physics of Plasmas* 7.6 (2000), pp. 2594–2603. DOI: 10.1063/1.874101. eprint: https://doi.org/10.1063/1.874101. URL: https://doi.org/10.1063/1.874101.

[10] K. Lan et al. "Octahedral spherical hohlraum and its laser arrangement for inertial fusion". In: *Physics of Plasmas* 21.5 (2014), p. 052704. DOI: 10.1063/1.4878835. eprint: https://doi.org/10.1063/1.4878835. URL: https://doi.org/10.1063/1.4878835.

[11] K. Lan and W. Zheng. "Novel spherical hohlraum with cylindrical laser entrance holes and shields". In: *Physics of Plasmas* 21.9 (2014), p. 090704. DOI: 10.1063/1.4895503. eprint: https://doi.org/10.1063/1.4895503. URL: https://doi.org/10.1063/1.4895503.

[12] K. Lan et al. "High flux symmetry of the Spherical Hohlraum with Octahedral 6 LEHs at the hohlraum-to-capsule radius ratio of 5.14". In: *Physics of Plasmas* 21 (2014). DOI: 10.1063/1.4863435.

[13] X. He and W. Zhang. "Advances in the national inertial fusion program of China". In: *EPJ Web of Conferences* 59 (2013), pp. 01009–. DOI: 10.1051/epjconf/20135901009.

[14] G. J. Balonek. "How Good is the Bright Ring Characterization for Uniformity of Deuterium Ice Layers within Cryogenic Nuclear Fusion Targets?" In: *LLE Summer High School Research Program* (2004). URL: http://www.lle.rochester.edu/media/publications/high_school_reports/documents/hs_reports/2004/Balonek_G.pdf.

[15] T. Mo. "X-Ray Backlighting of Shock Ignition Experiments on the National Ignition Facility". In: *LLE Summer High School Research Program* (2010). URL: http://www.lle.rochester.edu/media/publications/high_school_reports/documents/hs_reports/2010/Mo_Tom.pdf.

[16] L. Jing et al. "Comparison of three hohlraum configurations with six laser entrance holes for indirect-drive inertial confinement fusion". In: *Nuclear Fusion* 58.9 (2018), p. 096017. DOI: 10.1088/1741-4326/aacec8. URL: https://doi.org/10.1088%2F1741-4326%2Faacec8.

[17] R. K. Kirkwood et al. "Observation of Energy Transfer between Frequency-Mismatched Laser Beams in a Large-Scale Plasma". In: *Phys. Rev. Lett.* 76 (1996), pp. 2065–2068. DOI: 10.1103/PhysRevLett.76.2065. URL: https://link.aps.org/doi/10.1103/PhysRevLett.76.2065.

[18] W. A. Farmer et al. "High-temperature hohlraum designs with multiple laser-entrance holes". In: *Physics of Plasmas* 26.3 (2019), p. 032701. DOI: 10.1063/1.5087140. eprint: https://doi.org/10.1063/1.5087140. URL: https://doi.org/10.1063/1.5087140.